

# Mapping brain-wide excitatory projectome of primate prefrontal cortex at submicron resolution and comparison with diffusion tractography

Mingchao Yan<sup>1,2†</sup>, Wenwen Yu<sup>3†</sup>, Qian Lv<sup>4</sup>, Qiming Lv<sup>1</sup>, Tingting Bo<sup>1,2</sup>, Xiaoyu Chen<sup>1,2</sup>, Yilin Liu<sup>1,2</sup>, Yafeng Zhan<sup>1,2</sup>, Shengyao Yan<sup>1,2</sup>, Xiangyu Shen<sup>1</sup>, Baofeng Yang<sup>3</sup>, Qiming Hu<sup>5</sup>, Jiangli Yu<sup>5</sup>, Zilong Qiu<sup>1</sup>, Yuanjing Feng<sup>5</sup>, Xiao-Yong Zhang<sup>3</sup>, He Wang<sup>3</sup>, Fuqiang Xu<sup>6</sup>, Zheng Wang<sup>4\*</sup>

<sup>1</sup>Institute of Neuroscience, State Key Laboratory of Neuroscience, Center for Excellence in Brain Science and Intelligence Technology, Chinese Academy of Sciences, Shanghai, China; <sup>2</sup>University of Chinese Academy of Sciences, Beijing, China; <sup>3</sup>Institute of Science and Technology for Brain-inspired Intelligence, Fudan University, Shanghai, China; <sup>4</sup>School of Psychological and Cognitive Sciences; Beijing Key Laboratory of Behavior and Mental Health; IDG/McGovern Institute for Brain Research; Peking-Tsinghua Center for Life Sciences, Peking University, Beijing, China; <sup>5</sup>College of Information Engineering, Zhejiang University of Technology, Hangzhou, China; <sup>6</sup>Shenzhen Key Lab of Neuropsychiatric Modulation and Collaborative Innovation Center for Brain Science, Guangdong Provincial Key Laboratory of Brain Connectome and Behavior, CAS Key Laboratory of Brain Connectome and Manipulation, Brain Cognition and Brain Disease Institute (BCBDI), Shenzhen Institutes of Advanced Technology, Shenzhen-Hong Kong Institute of Brain Science-Shenzhen Fundamental Research Institutions, Shenzhen, China

\*For correspondence:  
zheng.wang@pku.edu.cn

†These authors contributed  
equally to this work

**Competing interest:** The authors declare that no competing interests exist.

**Funding:** See page 23

**Received:** 27 July 2021

**Preprinted:** 15 September 2021

**Accepted:** 07 April 2022

**Published:** 20 May 2022

**Reviewing Editor:** Saad Jbabdi, University of Oxford, United Kingdom

© Copyright Yan, Yu *et al.* This article is distributed under the terms of the [Creative Commons Attribution License](https://creativecommons.org/licenses/by/4.0/), which permits unrestricted use and redistribution provided that the original author and source are credited.

**Abstract** Resolving trajectories of axonal pathways in the primate prefrontal cortex remains crucial to gain insights into higher-order processes of cognition and emotion, which requires a comprehensive map of axonal projections linking demarcated subdivisions of prefrontal cortex and the rest of brain. Here, we report a mesoscale excitatory projectome issued from the ventrolateral prefrontal cortex (vlPFC) to the entire macaque brain by using viral-based genetic axonal tracing in tandem with high-throughput serial two-photon tomography, which demonstrated prominent monosynaptic projections to other prefrontal areas, temporal, limbic, and subcortical areas, relatively weak projections to parietal and insular regions but no projections directly to the occipital lobe. In a common 3D space, we quantitatively validated an atlas of diffusion tractography-derived vlPFC connections with correlative green fluorescent protein-labeled axonal tracing, and observed generally good agreement except a major difference in the posterior projections of inferior fronto-occipital fasciculus. These findings raise an intriguing question as to how neural information passes along long-range association fiber bundles in macaque brains, and call for the caution of using diffusion tractography to map the wiring diagram of brain circuits.

## Editor's evaluation

This paper uses a novel technique in combination with high throughput microscopy to generate a detailed map of macaque prefrontal connections. It will not only be of interest to anatomists, but

also to the neuroimaging community, as it includes a detailed comparison to MRI-based connectivity approaches commonly used to study the human brain.

---

## Introduction

Higher-order processes of cognition and emotion regulation that depend on the prefrontal cortex are all based on multiple, long-range connections between neurons (*Neubert et al., 2014; Carlén, 2017; Borra et al., 2011*). Axons connecting local and distant neurons form a fundamental skeleton of the brain circuitry, which is of paramount importance to fathom the organization of in-/output pathways that enable those vital functions (*Oh et al., 2014; Zingg et al., 2014*). Given the complexity and heterogeneity of the primate prefrontal cortex (*Carlén, 2017*), understanding the working mechanisms of the prefrontal cortex requires a comprehensive map of axonal projections linking its demarcated subdivisions and the rest of brain. A subdivision of the prefrontal cortex - the ventrolateral section (vLPFC), which mainly spans Brodmann's Areas 44, 45 a/b, 46 v/f, and 12 r/l (*Saleem et al., 2014*), is central to a variety of functions including language, objective memory, and decision-making (*Sakagami and Pan, 2007; Levy and Wagner, 2011*). Emerging evidence further demonstrates abnormalities of vLPFC in tight association with deficits in cognitive flexibility (*Neubert et al., 2014; Cai et al., 2020; Zhan et al., 2021*), suggesting that an elaborate delineation of its hard wiring would shed light on the underlying neuropathology of psychiatric disorders (*Haber et al., 2020*).

Such neuroanatomical inter-areal connectivity has been probed using invasive bulk injections of tracers and noninvasive imaging methods with millimeter-scale spatial resolution (*Zeng, 2018; Glasser et al., 2016; Wang et al., 2013*). Histological neural tracing has been historically utilized for circuit/pathway mapping and continues to be the most reliable way of survey for all myelinated axons in mammalian brains (*Zeng, 2018; Luo et al., 2018; Bienkowski et al., 2018*), which has also been used as a gold standard to validate other modalities like diffusion tractography (*Schmahmann et al., 2007; Donahue et al., 2016; Reveley et al., 2015; Mortazavi et al., 2018; Folloni et al., 2019; Dyrby et al., 2018*). Diffusion tractography, which has been developed in the 1990s to estimate the tissue microstructure by means of spatial encoding of water molecule movements (*Basser et al., 1994*), represents the only methodology capable of inferring the ensemble of anatomical connections in the living animal or human brain (*Wedeen et al., 2012; Mori and Zhang, 2006*). But this technique is an indirect observation with limited resolution and accuracy, and its reliability of false negative and false positive findings remains to be fully validated in a 3D space (*Donahue et al., 2016; Maier-Hein et al., 2017*). Notably, some classic tract-tracing methods are not sensitive to specific neuronal types or axonal trajectories. They do not report the traveling course in a 3D space through which the axons travel for a remarkably long distance (i.e. over centimeter length). The pursuit of long-range axonal fiber tracing across the entire monkey brain has become feasible thanks to rapid advances in viral and genetic tools in the primate species, tissue labeling, large-scale microscopy, and computational image analysis (*Han et al., 2009; Nassi et al., 2015; Albanese and Chung, 2016; Bedbrook et al., 2018*). Moreover, viral-based techniques for targeting specific neuronal types in macaque brain have achieved remarkable success (*Han et al., 2009; Stauffer et al., 2016*), which may furnish the requisite biological detail including excitatory and inhibitory in-/output to enrich structural network reconstructions for improved prediction of brain function (*Suárez et al., 2020*). However, it remains unclear thus far what type of viral vector is suitable for long-range axonal fiber tracing (*Zeng, 2018; Luo et al., 2018*).

Cross-comparison of the fiber details generated by two modalities with spatial scale differences in order of magnitude is technically demanding as many cellular structures or fiber pathways of biological interest are rather small relative to the voxel size of most diffusion MRI data (*Mori and Zhang, 2006*). One of the challenging undertakings is to image long-range axonal fibers of many neurons with sufficiently high resolution to enable tracking axonal trajectories across the entire brain (*Ragan et al., 2012; Li et al., 2010*), which has stirred some debates such as right-angle fiber crossings (*Mortazavi et al., 2018; Wedeen et al., 2012*) and the existence of the inferior fronto-occipital fasciculus (IFOF) in the primate brain (*Forkel et al., 2014*). The IFOF first proposed in the early 19th century supposedly connects the ventrolateral prefrontal cortex and medial orbitofrontal cortex to the occipital lobe through the ventral part of the external capsule (*Curran, 1909; Catani et al., 2002*). Micro-dissection and diffusion MRI tractography studies have recently confirmed the anatomy of this

---

**eLife digest** In the brain is a web of interconnected nerve cells that send messages to one another via spindly projections called axons. These axons join together at junctions called synapses to create circuits of nerve cells which connect neighboring or distant brain regions. Notably, long-range neural connections underpin higher-order cognitive skills (such as planning and emotion regulation) which make humans distinct from our primate relatives. Only by untangling these far-reaching networks can researchers begin to delineate what sets the human brain apart from other species.

Researchers deploy a range of imaging techniques to map neural networks: scanning entire brains using MRI machines, or imaging thin slices of fluorescently labelled brain tissue using powerful microscopes. However, tracing long-range axons at a high resolution is challenging, and has stirred up debate about whether some neural tracts, such as the inferior fronto-occipital fasciculus, are present in all primates or only humans.

To address these discrepancies, Yan, Yu et al. employed a two-pronged approach to map neural circuits in the brains of macaques. First, two techniques – called viral tracing and two-photon microscopy – were used to create a three-dimensional, fine-grain map showing how the ventrolateral prefrontal cortex (vlPFC), which regulates complex behaviors, connects to the rest of the brain. This revealed prominent axons from the vlPFC projecting via a single synapse to distant brain regions involved in higher-order functions, such as encoding memories and processing emotion. However, there were no direct, monosynaptic connections between the vlPFC and the occipital lobe, the brain's visual processing center at the back of the head.

Next, Yan, Yu et al. used a specialized MRI scanner to create an atlas of neural circuits connected to the vlPFC, and compared these results to a technique tracing axons stained with a fluorescent dye. In general, there was good agreement between the two methods, except for major differences in the rear-end projections that typically form the inferior fronto-occipital fasciculus. This suggests that this long-range neural pathway exists in monkeys, but it connects via multiple synapses instead of a single junction as was previously thought.

The findings of Yan, Yu et al. provide new insights on the far-reaching neural pathways connecting distant parts of the macaque brain. It also suggests that atlases of neural circuits from whole brain scans should be taken with caution and validated using neural tracing experiments.

---

pathway (*Sarubbo et al., 2019; Barrett et al., 2020*). Despite an abundance of functional evidence supporting a central role of occipito-frontal circuitry in cognition and sensory integration, a number of axonal tracing studies, which have been able to identify monosynaptic connections, have failed to reveal the IFOF in the macaque brain (*Schmahmann et al., 2007; Schmahmann and Pandya, 2006*). By contrast, sparse connections between frontal and occipital cortices in macaques were reported by other labs (*Gerbella et al., 2010; Markov et al., 2014*), although they do not show whether these axons follow the course expected for the IFOF. As such, a detailed anatomical definition of the IFOF is a topic of active research (*Barrett et al., 2020*).

In the present study, we aim to establish a comprehensive brain-wide excitatory projectome of the vlPFC in macaque monkeys using viral-based genetic tracing in tandem with serial two-photon (STP) tomography (*Figure 1A*), a technique that has successfully achieved high-throughput fluorescence imaging of the entire mouse brain by integrating two-photon microscopy and tissue sectioning (*Ragan et al., 2012*). We also performed ex vivo dMRI scans of the entire macaque brains to track the axonal fiber tracts using an ultra-high field (11.7T) MRI scanner (*Figure 1C*). In addition, in a common 3D space (*Figure 1B*), we intended to make a direct comparison of the mesoscale projectome to that derived from ultra-high field diffusion tractography (*Figure 1C and D*).

## Results

### Determination of viral vectors for long-range anterograde tracing

We tested whether VSV, lentivirus, and AAV vectors with demonstrated success in rodents worked in the macaque brain and which vector was best suitable for long-range axonal fiber tracing. Five days after infection with VSV- $\Delta$ G, the neuronal cell bodies in the cerebral cortex (*Figure 2A and B*)

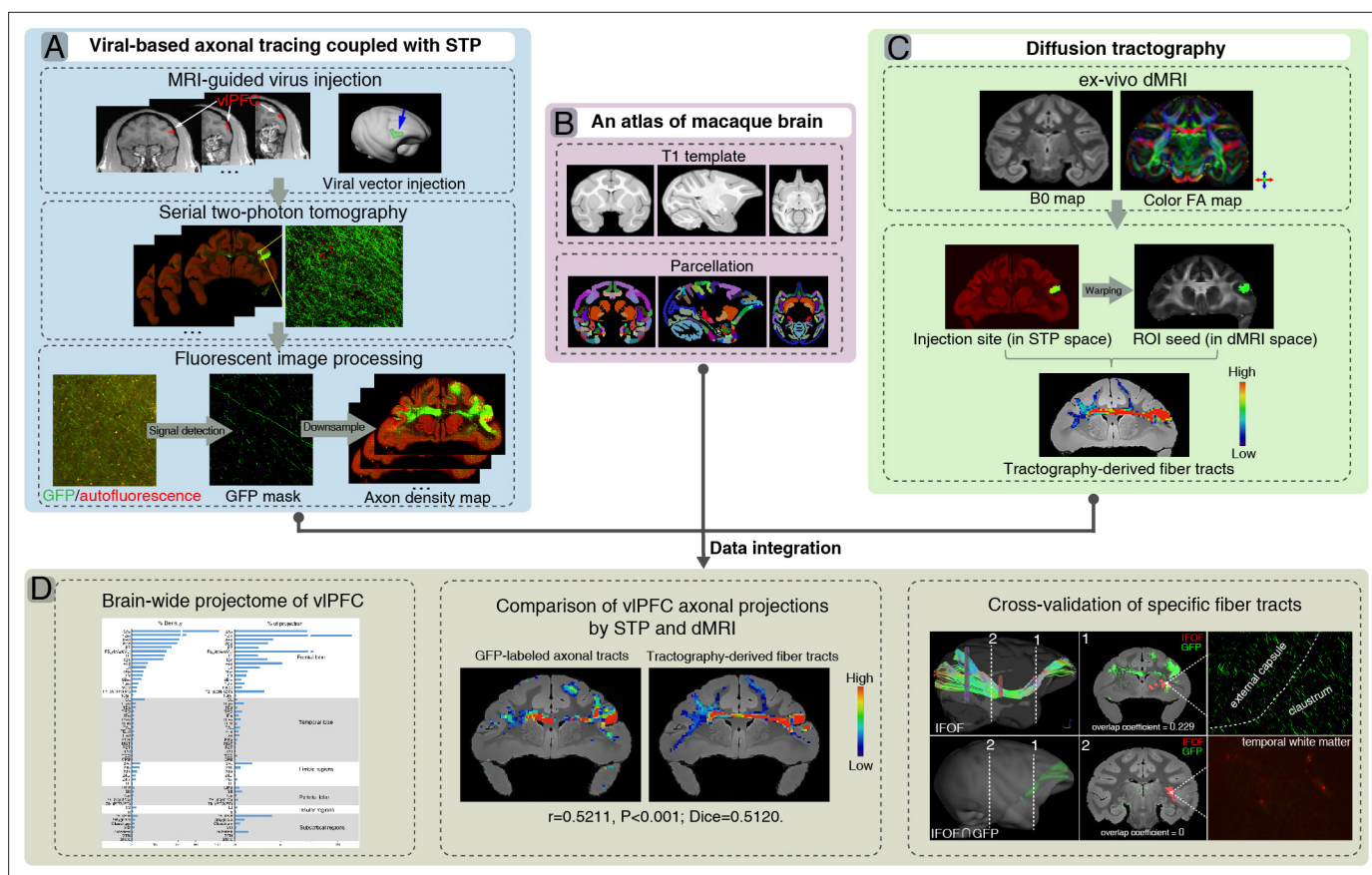


**Figure 1.** A flowchart diagram for brain-wide analyses of ventrolateral prefrontal cortex (vIPFC) projectome in macaques. The pipeline integrates the serial two-photon (STP) data in the mesoscopic domain (A) with macroscopic dMRI data (C) in a common 3D space (B). (A) T1 images were used to guide stereotaxic injection of AAV vectors to vIPFC (upper panel). High-throughput fluorescent images of viral-based genetic axonal tracing were acquired by STP tomography throughout the brain, which enables a close-up view and quantitative analysis of any region of interest (middle panel). A supervised machine learning approach was used for segmentation of GFP-positive signal and removal of autofluorescence in STP data. The serial segmented GFP images were down-sampled to compute the total signal intensity for each  $200\ \mu\text{m} \times 200\ \mu\text{m}$  grid by summing the number of signal-positive pixels in that grid and to generate the axonal density map (bottom panel). (B) An MRI atlas of cynomolgus macaques was used to construct a common 3D space. (C) Ex-vivo dMRI of macaque brain was acquired using an 11.7T MRI scanner, illustrated as representative B0 (left) and direction-encoded color FA maps (right). Using the injection site identified from the STP data as seed regions, the target fiber tracts can be derived from diffusion tractography. (D) Integration of STP and dMRI data was implemented in a common 3D space, which allows quantitative analyses including whole-brain analysis of axonal projectome (left), comparison of vIPFC projectome by STP and dMRI (middle), and cross-validation of fiber tracking in both STP and dMRI (right).

The online version of this article includes the following figure supplement(s) for figure 1:

**Figure supplement 1.** A customized setup of serial two-photon tomography for macaque brain.

**Figure supplement 2.** A typical STP tomography image set of a single macaque brain.

**Figure supplement 3.** Autofluorescence in macaque brain.

**Figure supplement 4.** Difference between axonal varicosities and dot-looking background.

**Figure supplement 5.** Co-registration of STP images to the MRI-based template of macaque brain.

**Figure supplement 6.** Representative fluorescent images showing injection site and major tracts of sample #7.

and mediodorsal (MD) thalamus (Figure 2—figure supplement 1A) were clearly labeled with GFP, although only proximal neurites were labeled with no long-range axonal fibers detected (Figure 2—figure supplement 2). When the infection time was extended to about a month, we observed widespread axon loss and neuronal cell death (Figure 2—figure supplement 1D-G). The long-term-infected neurons underwent morphological changes such as membrane blebbing (Figure 2—figure supplement 1B and C), a key morphological change associated with the induction of apoptosis. Local

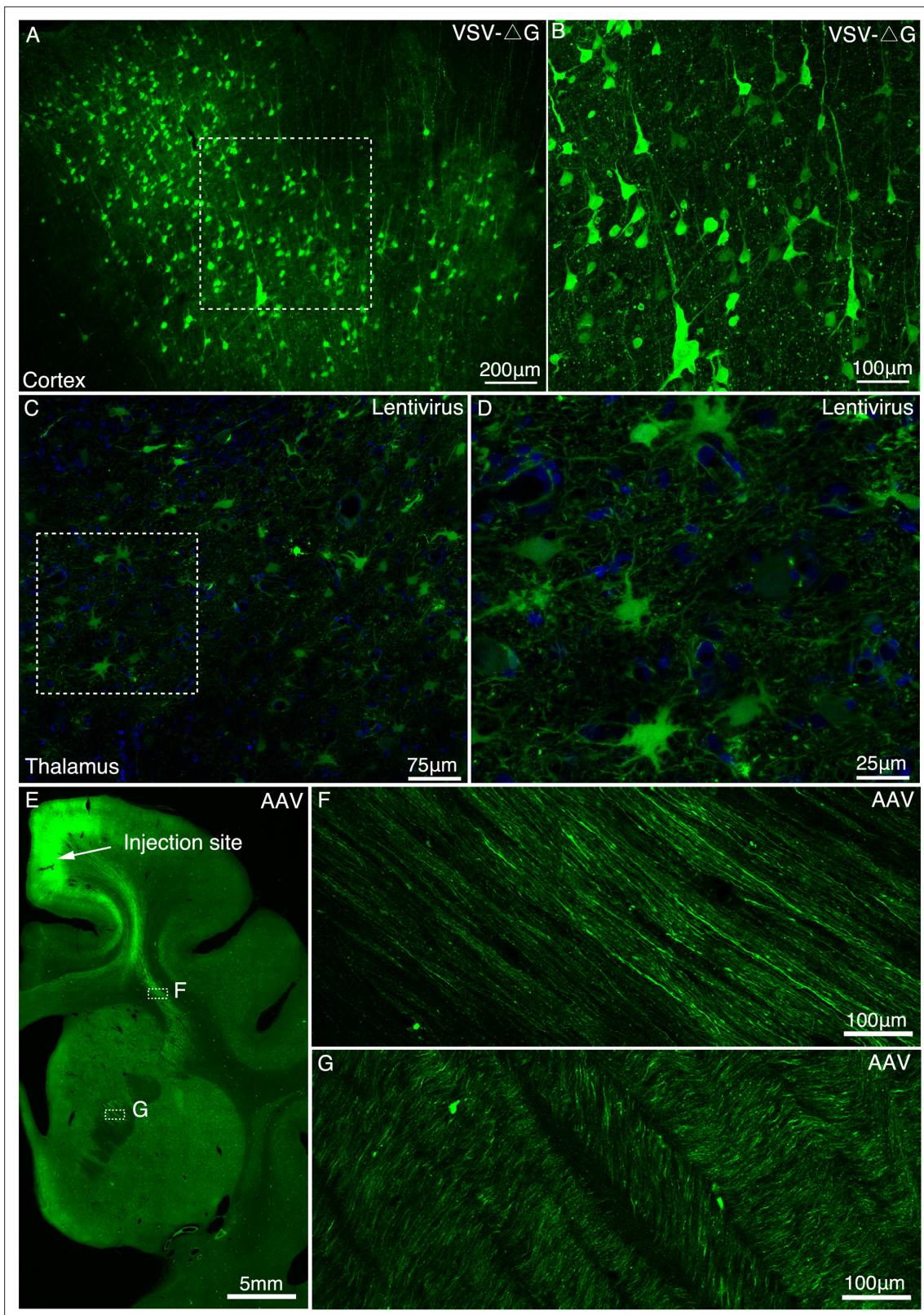


**Figure 2.** Determination of viral vectors for long-range anterograde tracing in macaques. **(A)** GFP-labeled neurons were found in the premotor cortex ~5 days after injection of VSV- $\Delta$ G encoding Tau-GFP. **(B)** A magnified view illustrating the morphology of GFP-labeled neurons in the area outlined with a white box in **(A)**. **(C)** Lentivirus construct was injected into the macaque thalamus and examined for transgene expression after ~9 months. **(D)** High power views of the dotted rectangle in panel **C**. **(E)** GFP-labeled neurons and axons were observed in the premotor cortex ~45 days after injection of

*Figure 2 continued on next page*

Figure 2 continued

AAV2/9 encoding Tau-GFP. Two dashed line boxes enclose the regions of interest: frontal white matter and ALIC, whose GFP signal are magnified in (F) and (G), respectively.

The online version of this article includes the following figure supplement(s) for figure 2:

**Figure supplement 1.** Long-term expression of VSV-ΔG induced neurotoxicity in macaque brain.

**Figure supplement 2.** Expression of GFP using VSV-ΔG injected into the MD thalamus of macaque brain.

**Figure supplement 3.** Expression of GFP using lentivirus injected into the MD thalamus of macaque brain.

**Figure supplement 4.** Expression of GFP using AAV2/9 injected into the MD thalamus of macaque brain.

**Figure supplement 5.** AAV-infected cells were stained for NeuN and GFAP antibodies.

**Figure supplement 6.** Comparison of two AAV constructs.

**Figure supplement 7.** Long-range axonal tracing outcomes using AAV2/9, lentivirus, and VSV-ΔG.

injection with VSV-ΔG mediated rapid and transient gene expression nearby the injection site, and an extension of infection time evidently caused fatal neurotoxicity.

Lenti-Ubic-GFP exhibited stable expression in the cell soma even after 9 months (**Figure 2C and D**), despite sparse labeling of GFP positive axons (**Figure 2—figure supplement 3**). By contrast, 6 weeks after AAV2/9-CaMKIIa-Tau-GFP was injected into the premotor cortex (**Figure 2E-G**) or MD thalamus (**Figure 2—figure supplement 4**), axonal fiber bundles like anterior limb of internal capsule (ALIC) (**Figure 2G**) were clearly visualized over several centimeters. The AAV-infected cells were positive for the neuronal specific marker NeuN, but negative for astrocyte specific marker GFAP (**Figure 2—figure supplement 5**). As a validation test, AAV2/9 construct encoding mCherry was co-injected with AAV2/9 construct encoding Tau-GFP into the premotor cortex. And we found that the signal intensity of most Tau-GFP labeled axons was consistently higher than that of mCherry labeled axons (**Figure 2—figure supplement 6A-D**).

We compared the axonal fiber tracing efficiency of VSV-ΔG, Lentivirus and AAV2/9 (AAV2/9-CaMKIIa-Tau-GFP) in the MD thalamus (**Figure 2—figure supplement 7**). The density of axonal fibers labeled by AAV2/9 (**Figure 2—figure supplement 7C**) was significantly higher ( $P < 0.001$ , **Figure 2—figure supplement 7D**) than by Lentivirus (**Figure 2—figure supplement 7B**) and VSV-ΔG (**Figure 2—figure supplement 7A**). VSV-ΔG labeled axons sparse in the proximal, and the axonal density decreased sharply (**Figure 2—figure supplement 7D**). Axons labeled by lentivirus (**Figure 2—figure supplement 7B**) were also significantly denser ( $P < 0.01$ , **Figure 2—figure supplement 7D**) than by VSV-ΔG (**Figure 2—figure supplement 7A**) distant from the injection site.

## Brain-wide excitatory projectome of vIPFC in macaques

AAV2/9 encoding Tau-GFP under the control of excitatory promoter CaMKIIa was determined as an anterograde tracer for mapping the excitatory projectome of vIPFC. The injection site in vIPFC, validated by STP images, including area 45, 12 l, and 44, was precisely located in cortical gray matter (**Figure 4A-D**). To identify the cell type specificity of Tau-GFP gene expression driven by the CaMKII- $\alpha$  promoter, immunofluorescent staining was performed with antibodies against the excitatory neuron specific marker CaMKII- $\alpha$  and the inhibitory neuron-specific neurotransmitter GABA. GFP-positive neurons in the injection site were observed positive for CaMKIIa (**Figure 4—figure supplement 1A-C**) and negative for GABA (**Figure 4—figure supplement 1D-F**), indicating that the AAV labeled neurons were glutamate excitatory neurons.

To acquire a detailed account of the brain-wide vIPFC projectome, we analyzed its connectivity profile with other 173 parcellated regions in the monkey brain atlas using the STP tomography data (**Figures 3 and 4**). The GFP-labeled projecting axons largely encompassed the anterior part of the brain including the frontal lobe, temporal lobe, limbic regions, insular, and some subcortical regions, but no labeled axons were found in the occipital lobe (**Figure 3A-C**, **Figure 3—figure supplement 1**). Within the frontal lobe, GFP-labeled projecting axons were markedly dense in the OFC, rostrally distributed in area 12 m (**Figure 4E, F and G**), 12o (**Figure 4E**), 11 l (**Figure 4E, H and I**), 13 l (**Figure 4E**), and 13 m (**Figure 4E**). The 12 m received strongest innervation from vIPFC relative to other OFC subregions (**Figure 4E**). Laterally, axonal projections were found in the FEF including 8Av (**Figure 4—figure supplement 2A, B and C**) and 8Ad (**Figure 4—figure supplement 2A and D**).

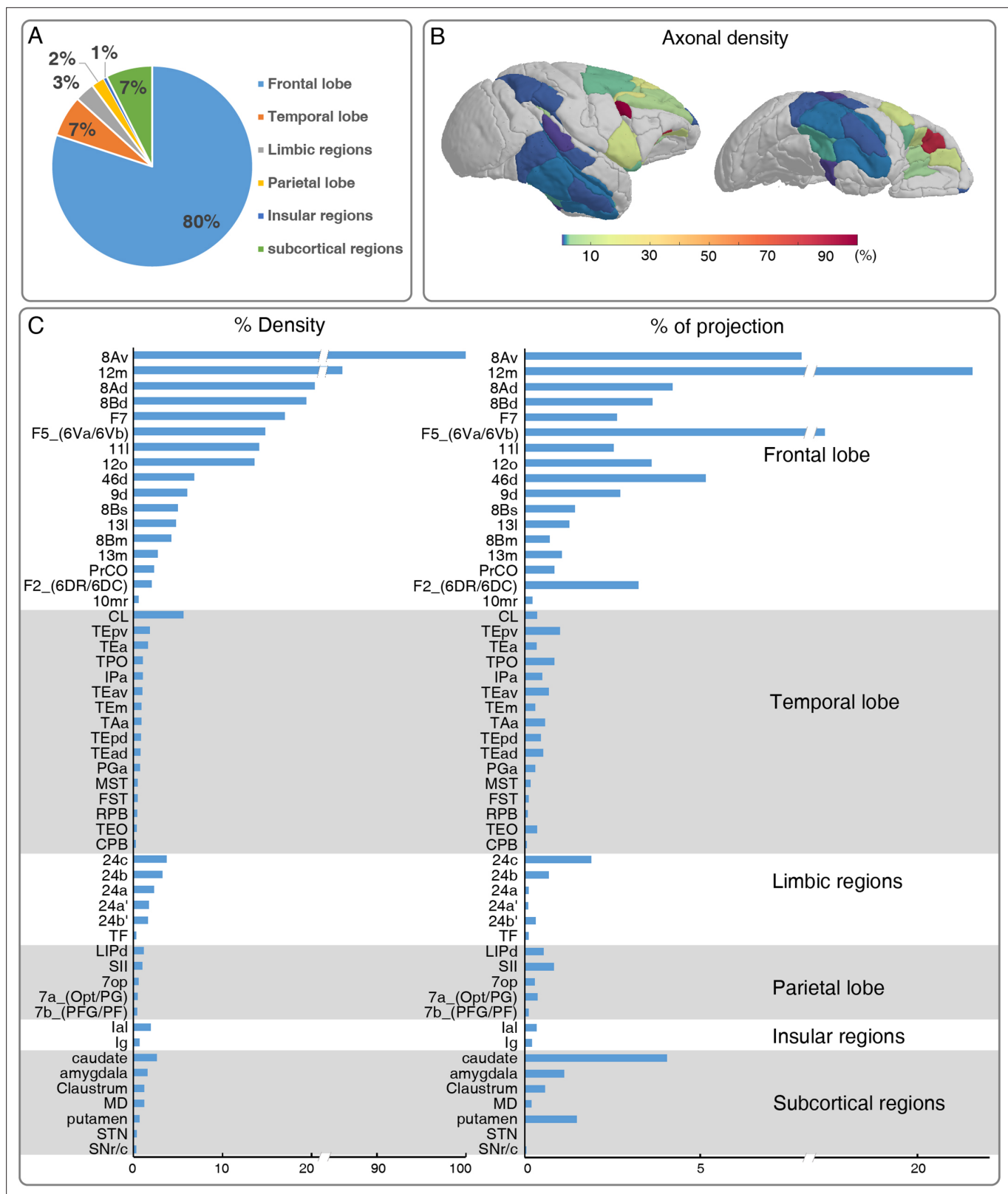


**Figure 3.** Brain-wide distribution of GFP-labeled excitatory projectome of ventrolateral prefrontal cortex (vIPFC). **(A)** A pie chart shows the brain-wide distribution of vIPFC axonal projectome. **(B)** The normalized percentage distribution of axonal density was rendered onto a 3D brain surface. **(C)** The histogram plots show the vIPFC projections to other regions where the connectivity strength was quantified by the density of GFP-positive axons and proportion of total projection. We calculated the innervation density, given in percent of strongest projection.

Figure 3 continued on next page

Figure 3 continued

The online version of this article includes the following source data and figure supplement(s) for figure 3:

**Source data 1.** Entire dataset for the brain-wide distribution of vIPFC axonal projectome used in **Figure 3**.

**Figure supplement 1.** Drawings of coronal sections showing the distribution of the anterograde viral labeling after the injection in vIPFC (Case #8).

Dorsally, there were dense axonal fibers in the dorsal prefrontal cortex, including area 8Bd (**Figure 4—figure supplement 2E, F and G**), 8Bm (**Figure 4—figure supplement 2E**), 8Bs (**Figure 4—figure supplement 2E**), 46d (**Figure 4—figure supplement 2E, H and I**), and 9d (**Figure 4—figure supplement 2E, J and K**). The 8Bd and 46d received relatively more innervation compared with 9d, 8Bs, and 8Bm (**Figure 4—figure supplement 2E**). On the medial surface of the brain, scattered axon fibers were visible in area F5 (**Figure 4—figure supplement 2L and M**), F7 (**Figure 4—figure supplement 2L and N**), and F2 (**Figure 4—figure supplement 2L**) of the premotor cortex. The axons with the premotor cortex exhibited a gradient pattern with the largest axon distribution along the anterior part (**Figure 4—figure supplement 2L**). In addition, axons were noted in the precentral opercular area (PrCO) and medial prefrontal area (mainly in 10mr) (**Figure 3C**). Interestingly, the projections anchored in the prefrontal cortex of these axonal fibers formed isolated clusters (**Figure 4F and H**, indicated by arrows). The z-axis extent of axonal clusters was ranging from 1.2 mm to 3.8 mm ( $2.24 \pm 0.80$  mm) (**Figure 4—figure supplement 3**).

Beyond the frontal lobe, rich connections were observed in the temporal lobe (**Figure 3**), predominantly in caudal lateral (CL), caudal (CPB), and rostral (RPB) portions of parabelt region of the auditory cortex; anterior TE (TEa), medial TE (TEm), superior temporal polysensory area (STP, correspond to areas PGa and TPO), IPa and TAa of the dorsal bank/ventral bank/fundus of the superior temporal sulcus (STSd/v/f) (**Figure 3C**); medial superior temporal area (MST), floor of superior temporal area (FST), anteroventral TE (TEav), anterodorsal TE (TEad), and area TEO of superior temporal area. The vIPFC also sends axons to limbic regions, mainly in 24 a, 24 a', 24b, 24b', and 24 c of anterior cingulate areas (ACC) (**Figure 3C**); area TF of parahippocampal cortex (**Figure 3C**). Relatively weak projections were observed in the dorsal subdivision of lateral intraparietal area (LIPd); 7 a and 7b of inferior parietal lobule areas; secondary somatosensory area (SII) and parietal operculum (7op) of the parietal cortex (**Figure 3C**). There were some sparsely labeled axons in the granular insula (Ilg) and lateral agranular insula (Ial) area (**Figure 3C**). In white matter, traveling axonal bundles were found in the corpus callosum, anterior limb of internal capsule (ALIC, **Figure 4—figure supplement 4A, B**), and anchored into the MD thalamus (**Figure 4—figure supplement 4C, D**). Subcortically, axon clusters were observed in the medial (**Figure 4—figure supplement 4F, G**) and caudal (**Figure 4—figure supplement 4H**) parts of caudate. High resolution confocal images revealed that axons in MD (**Figure 4—figure supplement 4D**) and caudate (**Figure 4—figure supplement 4J**) were thinner than those in the ALIC (**Figure 4—figure supplement 4B**). Furthermore, the labeled axons were found extending to the parvocellular part of accessory basal nucleus of amygdala (ABpc), reticulate and compacta parts of substantia nigra (SNr/c), claustrum and subthalamic nucleus (STN) (**Figure 3C**).

### Comparison of vIPFC axonal projections by dMRI and STP

We further introduced a quantitative comparison of vIPFC connectivity profile obtained by dMRI-based tractography and STP data. Typical T2-weighted and dMRI images of the macaque brain acquired from an ultra-high field MRI scanner were shown in **Figure 5A–D**. GFP projection and probabilistic tract were plotted with the Dice coefficients and Pearson coefficients (R) along the anterior-posterior axis of the whole macaque brain. The Dice coefficients and Pearson coefficients were higher in dense projection regions, especially for the vIPFC-CC-contralateral tract (**Figure 6A**). To carry out a proof-of-principle investigation, we focused on the vIPFC-CC-contralateral tract that was reconstructed in 3D space by using STP and dMRI data, respectively (**Figure 6B and C**). After co-registering the reconstructed tracts into a common 3D space, our approach relied on slice-based statistical correlation methods (the Pearson correlation and Dice coefficients) along this vIPFC-CC-contralateral tract. Upon visual comparison, the dMRI-derived tracts largely overlapped with the axonal bundles shown in STP images (**Figure 6B and C**). Statistical correlation indices were computed for each pair of diffusion tractography and STP images to quantify their spatial overlap. We found consistent, marked agreement between these two modalities along this tract, as demonstrated in **Figure 6D–F**. For all slices (spaced



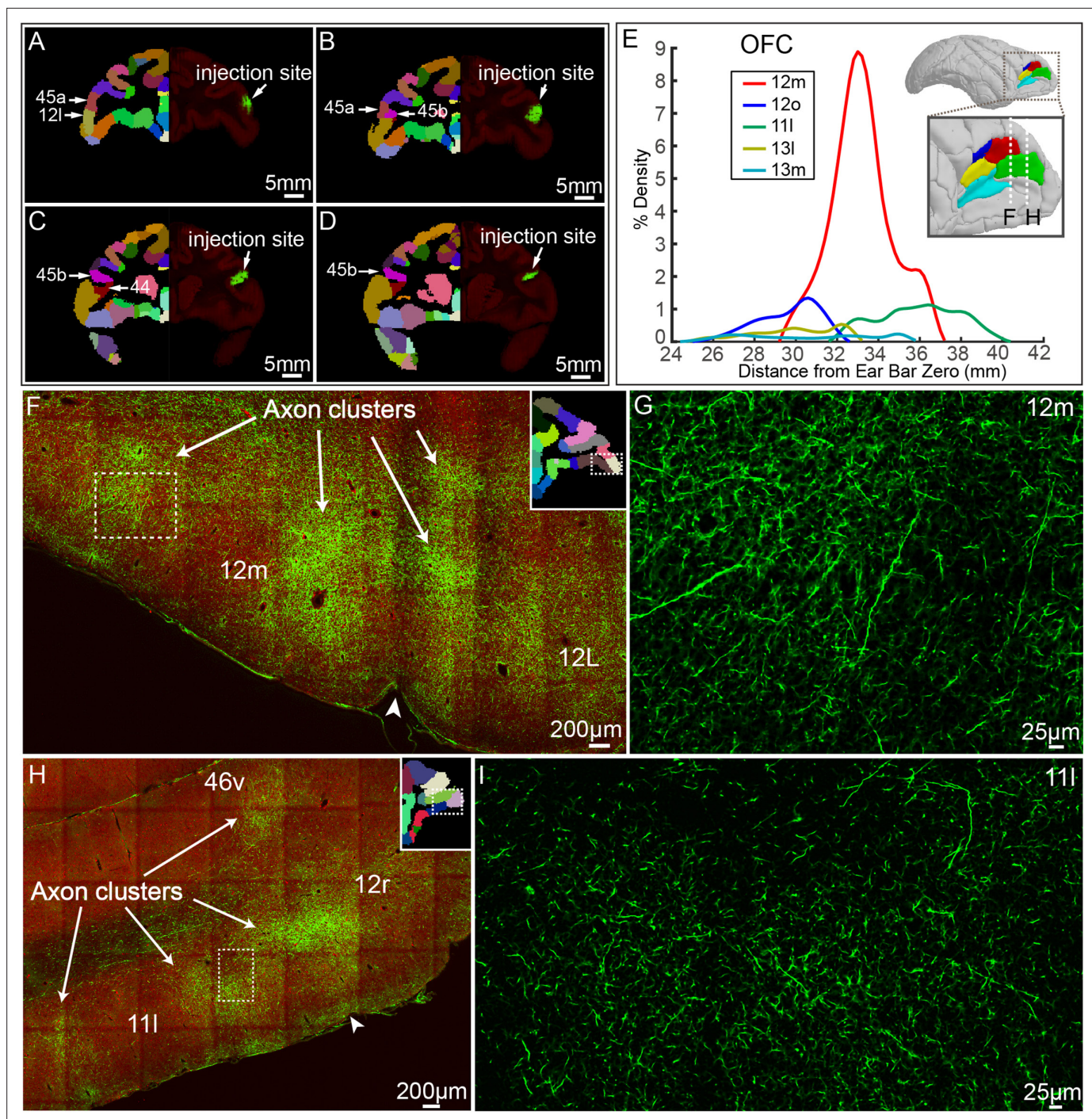


**Figure 4.** ventrolateral prefrontal cortex (vIPFC) projectome within the prefrontal lobe. (A–D) Representative coronal slices of the injection site in vIPFC are shown overlaid with the monkey brain template (left hand side), mainly spanning areas 45 a, 45b, 12 l, and 44. (E) Percentage of output density of vIPFC projectome along the anterior-posterior axis of the OFC. The inset shows the spatial location of individual Brodmann areas in OFC. Dotted lines indicate anterior-posterior position of the following fluorescent images. (F–I) Representative two-photon images of vIPFC axonal projections to OFC: 12 m and 11 l. Arrows indicate the axon clusters. Insets show the low power images of the section indicating the position of the higher power images.

The online version of this article includes the following figure supplement(s) for figure 4:

**Figure supplement 1.** Expression of Tau-GFP in excitatory neurons in macaque brain.

**Figure supplement 2.** Representative cortical projections of vIPFC.

**Figure supplement 3.** The spatial extent of axonal clusters in the frontal cortex.

**Figure supplement 4.** Representative subcortical projections of vIPFC.

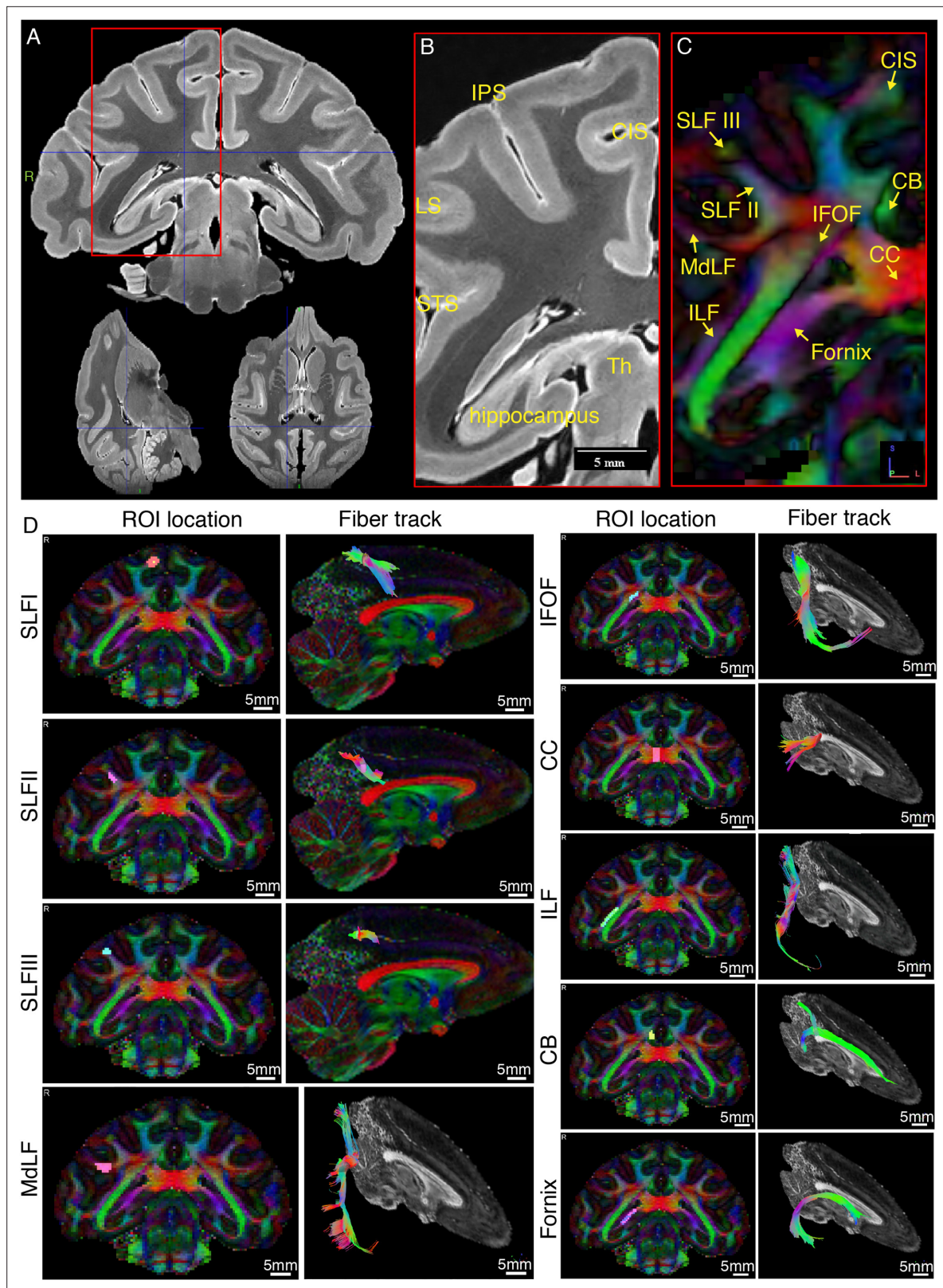


**Figure 5.** Representative *ex-vivo* MRI images of macaque brain. (A) Typical high-resolution T2-weighted images were shown in axial, coronal, and sagittal planes. (B) Zoom-in view of the red box in panel A, shown with anatomical landmark gyri including intraparietal sulcus (IPS), lunate sulcus (LS), superior temporal sulcus (STS), and cingulate sulcus (CIS). (C) The color-coded FA map corresponding to B. Major fiber bundles including superior longitudinal fasciculus subcomponent I, II, and III (SLF-I, -II, -III), inferior fronto-occipital fasciculus (IFOF), inferior longitudinal fasciculus (ILF), middle

Figure 5 continued on next page

Figure 5 continued

longitudinal fasciculus (MdLF), corpus callosum (CC), cingulum bundle (CB), and fornix are clearly demonstrated. Red color codes left and right, blue color codes superior and inferior, and green color codes anterior and posterior directions. (D) Typical tractography of the main fiber bundles indicated in C are derived from the present dMRI data. The ROI locations and fiber tracks are overlaid on the color-coded FA maps.

by 500  $\mu\text{m}$ ) along vIPFC-CC-contralateral tract, we observed consistent and significant correlations between these two modalities ( $R = 0.4624 \pm 0.0922$ ; Dice =  $0.4312 \pm 0.0861$ ). Two example GFP-labeled axon images as marked in **Figure 6F** were displayed in **Figure 6G–J** with different magnifications, showing typical traveling axons in corpus callosum (**Figure 6G and H**) and frontal white matter (**Figure 6I and J**).

### Inferior fronto-occipital fasciculus in macaques

As illustrated by diffusion tractography, the inferior fronto-occipital fasciculus (IFOF) in macaques is a long-ranged bowtie-shaped tract (**Figure 7A**), showing traveling course similar to humans. The frontal stem of IFOF spread to form a thin sheet, and its temporal stem narrowed in coronal section, mainly gathered at the external capsule. The intersection between IFOF and axonal projections of vIPFC was shown in a common 3D space of diffusion tractography in **Figure 7B**, whereby the posterior part of vIPFC axonal projections apparently ends at the middle superior temporal region, far from the occipital lobe. To quantify the spatial correspondence between the IFOF tract and vIPFC projectome, the Szymkiewicz-Simpson overlap coefficient was calculated in a shared common 3D space after co-registration. It was 0.0397 and 0.0535 in 3D space for two dMRI data sets, indicating that only a small fraction of the IFOF tract and vIPFC projectome overlapped (mainly in the front half of the brain, **Figure 7**). Also, the Szymkiewicz-Simpson overlap coefficients between 2D coronal slices of IFOF and vIPFC projectome were plotted along the anterior-posterior axis of the macaque brain (**Figure 7C**). The anterior part of the vIPFC axonal projections shown by STP tomography largely overlapped with the dMRI-derived IFOF tracts in frontal whiter matter (**Figure 7D**), external capsule (**Figure 7E**), claustrum (**Figure 7E and F**), and extreme capsule (**Figure 7F**). Meanwhile, the posterior part of dMRI-derived IFOF tract passed through temporal white matter (**Figure 7G**), whereas the posterior part of fiber projections of vIPFC sent no axons to this region (**Figure 7G**).

We observed SLFIII linking the inferior parietal lobe to frontal lobe by traveling horizontally through the white matter in the macaque brain (**Figure 7—figure supplement 1A**). The spatial trajectory of SLFIII derived from dMRI tractography was validated through the comparison of virally labeled axonal fibers. Most axonal fibers of the SLFIII tract travel perpendicular to the coronal plane (cutting plane) such that these labeled fibers appeared mainly as green dots in high magnification fluorescent images (**Figure 7—figure supplement 1B–G**). Similarly, we calculated the Szymkiewicz-Simpson overlap coefficients between the SLFIII derived from diffusion tractography and the parietal branch of vIPFC projections identified from viral tracing in two brain samples, as showed markedly high overlap ( $r = 0.2603$  and  $0.2175$ ). Unlike the IFOF in which the results of diffusion tractography mainly overlapped with those of viral tracing in the anterior part (**Figure 7**), the dMRI-derived SLFIII substantially overlapped with the vIPFC axonal projections in frontal and parietal whiter matter along the whole trajectory (**Figure 7—figure supplement 1**).

## Discussion

### Brain-wide excitatory projectome of vIPFC in macaques

We customized STP tomography for whole-brain imaging of the macaque monkey at submicron resolution and accomplished brain-wide 3D reconstruction of axonal connectome, thanks to prominent characteristics of STP tomography including free of tissue distortions, no need for section-to-section alignment, and high-resolution image sets readily warped in 3D space (**Amato et al., 2016**). Importantly, we coupled STP tomography with genetic methods using enhancers/promoter elements that target specific cell types (**Luo et al., 2018**). Previous studies have demonstrated that a CaMKII $\alpha$  promoter carried by lentivirus was able to target excitatory neurons with optogenetic proteins in the macaque brain (**Han et al., 2009**), and a TH promoter carried by AAV selectively targeted dopamine neurons (**Stauffer et al., 2016**). Here we deployed AAV with CaMKII $\alpha$  promoter to focus on the

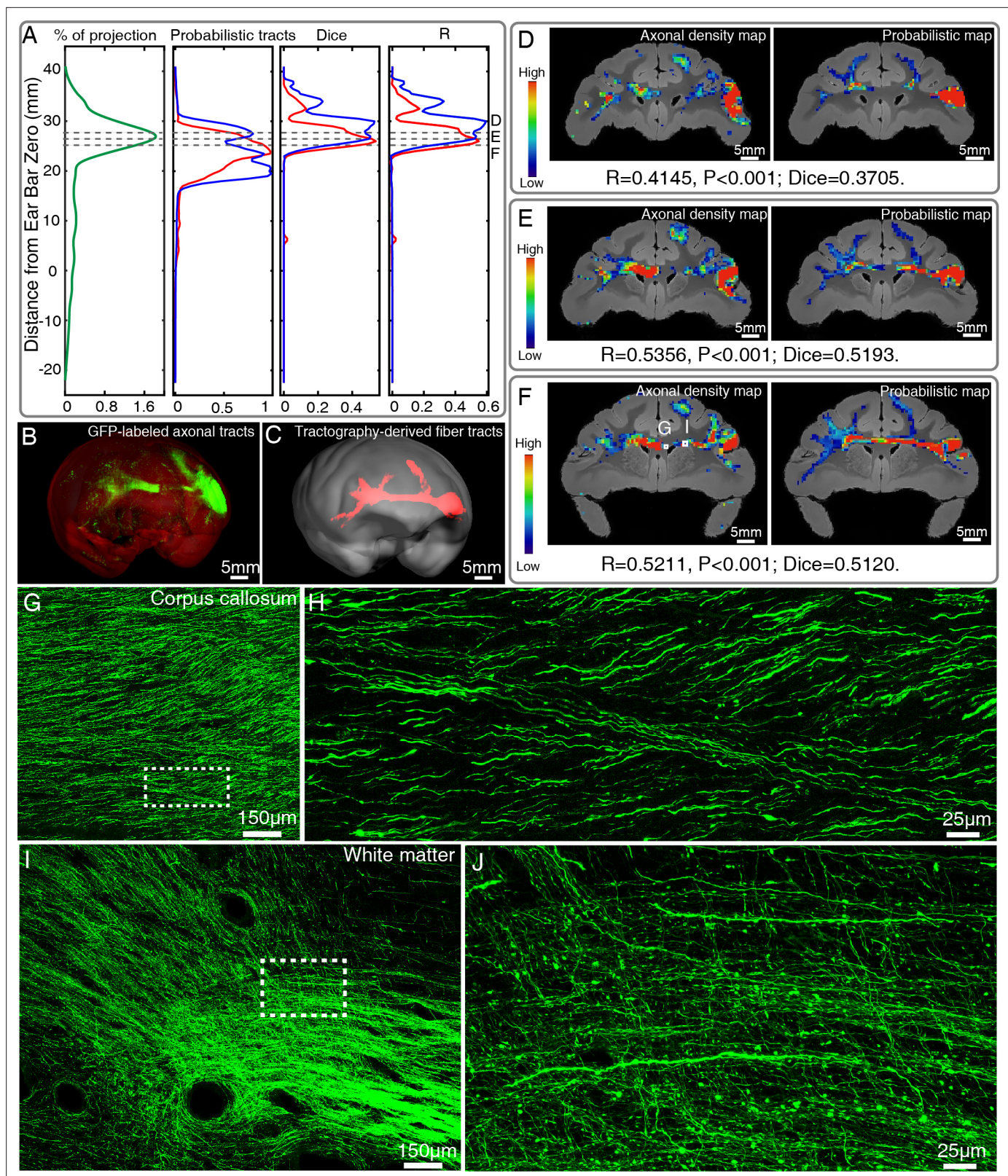


**Figure 6.** Comparison of ventrolateral prefrontal cortex (vIPFC) connectivity profiles by serial two-photon (STP) tomography and diffusion tractography. **(A)** Percentage of projection, Probabilistic tracts, Dice coefficients, and Pearson coefficients (**R**) were plotted along the anterior-posterior axis in the macaque brain. Blue and red colors indicate results of two dMRI data sets acquired from different macaque monkeys. **(B, C)** 3D visualization of the fiber tracts issued from the injection site in vIPFC to corpus callosum to the contralateral vIPFC by STP tomography and diffusion tractography.

Figure 6 continued on next page

Figure 6 continued

(D–F) Representative coronal slices of the diffusion tractography map and the axonal density map along the vIPFC-CC-contralateral tract, overlaid with the corresponding anatomical MR images. (G–J) GFP-labeled axon images as marked in (F) were shown with magnified views. (H, J) correspond to high magnification images of the white boxes indicated in G and I, both of which presented a great deal of details about axonal morphology.

excitatory projection of vIPFC, whereby immunofluorescent staining with both CaMKII $\alpha$  and GABA confirmed that GFP was specifically expressed in excitatory neurons. Hence, this integrated approach allows clear dissection of projection patterns from diverse neuronal types (Bedbrook et al., 2018), and enriches our knowledge about the anatomical infrastructure of neural circuits for individual cell types at the entire brain scale (Stauffer et al., 2016).

Both anterograde and retrograde tracing evidence shows that vIPFC is extensively connected to other divisions of PFC including OFC, FEF, and the ventral premotor cortex. Extrinsic connections beyond the PFC, vIPFC is connected mainly to the dysgranular insula, frontal operculum, somatosensory-related areas in the parietal operculum and inferior parietal cortex, visual-related areas in the inferior temporal cortex, and anterior cingulate areas (Saleem et al., 2014; Gerbella et al., 2010). We found the excitatory projection of vIPFC to the rest of brain was compatible with previous reports using chemical tracers (Borra et al., 2011; Gerbella et al., 2010; Safadi et al., 2018). Furthermore, we compared the current vIPFC projectome data with the well-known macaque connectivity database CoCoMac (Bakker et al., 2012), which includes the results of several hundred published axonal tract-tracing studies in the macaque monkey brain (Stephan, 2013). Essentially the vIPFC connectivity profile shown here was markedly similar to that of CoCoMac, except that vIPFC projections to PFCol, PFCdm, PFCdl, PFCoi, PFCm, PMCvl, amygdala, and SII have not been reported in CoCoMac database or reported merely with unspecified strength. In addition, we compared vIPFC projections with one recent report (Gerbella et al., 2010), showing that the brain regions projected from area 45 were clearly observed in the present vIPFC projection data. One recent study compared results of terminal labeling using Synaptophysin-EGFP-expressing AAV (specifically labeling synaptic endings) with the cytoplasmic EGFP AAV (labeling axon fibers and synaptic endings). There was high correspondence between synaptic EGFP and cytoplasmic EGFP signals in target regions (Oh et al., 2014). Thus, we relied on quantifying GFP-positive pixels (containing signals from both axonal fibers and terminals) rather than the number of synaptic terminals, similarly done in recent reports (Oh et al., 2014; Gehrlach et al., 2020).

### AAV2/9 is suitable for long-range axonal tracing in the macaque brain

Methods for tissue labeling have been continuously evolving from silver impregnation of degenerating fibers to ex-vivo visualization of axonally transported tracers injected at single brain nuclei, and finally to an integrated style which coupled high-resolution whole-brain imaging technologies with viral and genetic tracers (Nassi et al., 2015). Among four viral vectors tested here, we found that AAV2/9 demonstrated the highest efficiency of long-range axonal tracing in the macaque brain. VSV was initially utilized as a transsynaptic tracer in a previous study since VSV encodes five genes, including G protein which promotes anterograde transsynaptic spread among neurons (Beier et al., 2011). In our study, we used VSV with G deletions to trace axonal projection without trans-synaptic labeling, which enabled robust gene expression at remarkably higher level relative to other vectors in a very short time (less than a week). But we found that a shorter expression time of VSV- $\Delta$ G was insufficient to label axons traveling long distance whereas a longer expression time of VSV- $\Delta$ G caused cell death, consistent with a prior finding that VSV-G failed to label transsynaptic cells at distant areas (Mundell et al., 2015). The advantage of lentivirus, which is derived from human immunodeficiency virus type 1 (HIV-1) (Naldini et al., 1996), is that it has a large genetic capacity of approximately 10 Kb which allows for the expression of multiple gene and usage of more than one promoter or regulatory elements. And we found GFP expression induced by lentivirus remarkably stable after 9 months in macaque monkeys, even though the labeled level was mild (Schambach et al., 2013) and the labeled scope was limited.

As an effective carrier for gene delivery into the brain, AAV has a number of established advantages including minimal toxicity, weak host immune response, stable gene expression in neurons with extraordinarily high transfection efficiency (titers up to  $10^{12}$ – $10^{13}$  genome copies per mL) (Bedbrook

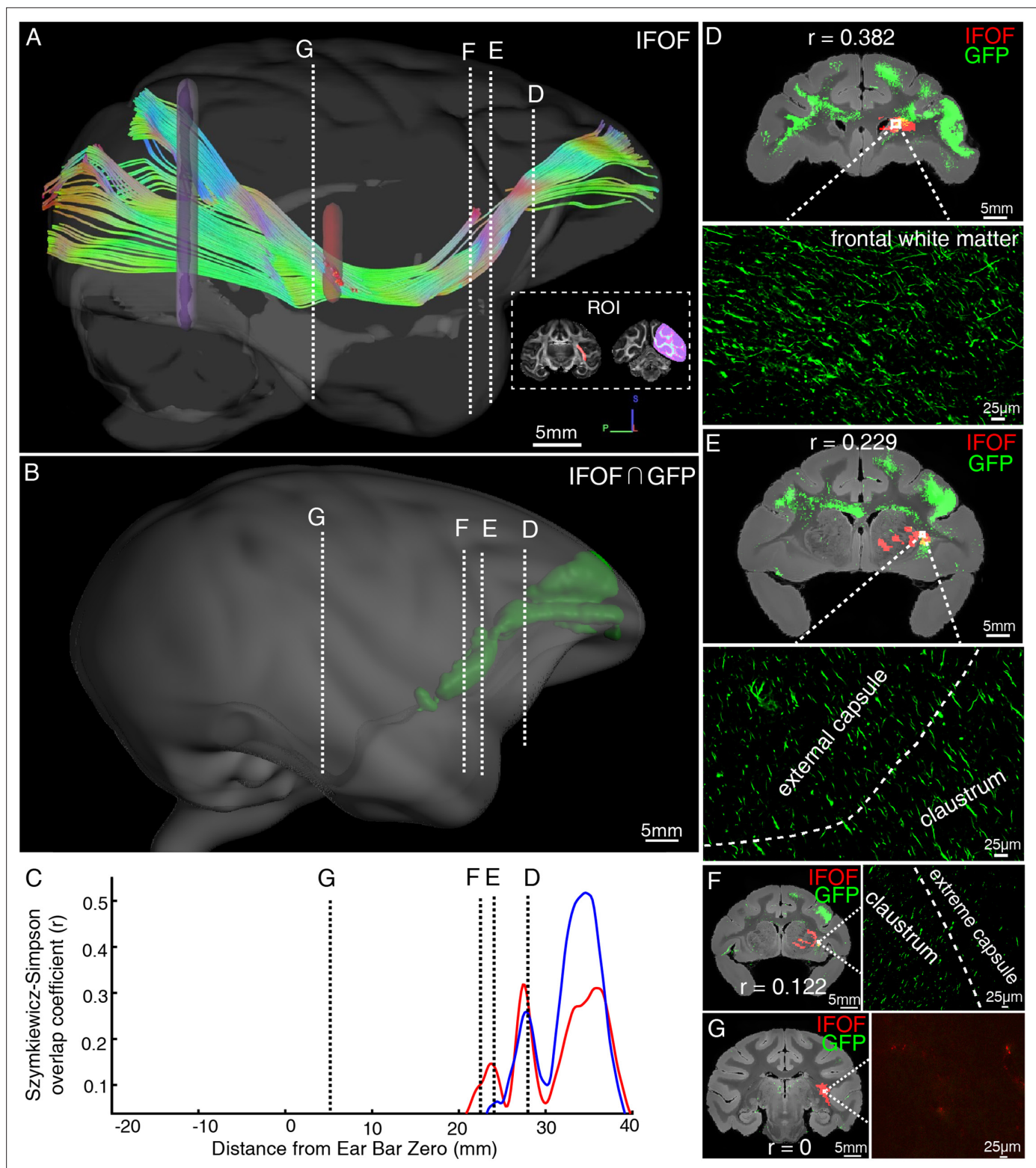


**Figure 7.** Illustration of the inferior fronto-occipital fasciculus by diffusion tractography and serial two-photon (STP) tomography. **(A)** The fiber tractography of inferior fronto-occipital fasciculus (IFOF) (lateral view). Two inclusion ROIs at the external capsule (pink) and the anterior border of the occipital lobe (purple) were used and shown on the coronal plane. The IFOF stems from the frontal lobe, travels along the lateral border of the caudate nucleus and external/extreme capsule, forms a bowtie-like pattern and anchors into the occipital lobe. **(B)** The reconstructed traveling course of IFOF based on vIPFC projectome was shown in 3D space. **(C)** The Szymkiewicz-Simpson overlap coefficients between 2D coronal brain slices of the dMRI-derived IFOF tract and vIPFC projections were plotted along the anterior-posterior axis of the macaque brain. Blue and red colors indicate results

Figure 7 continued on next page

Figure 7 continued

of two dMRI data sets acquired from different macaque monkeys. Four cross-sectional slices (D–G) along the IFOF tracts were arbitrarily chosen to demonstrate the spatial correspondence between the diffusion tractography and axonal tracing of STP images. (D–G) The detected GFP signals (green) of vIPFC projectome and the IFOF tracts (red) obtained by diffusion tractography were overlaid on anatomical MRI images, with a magnified view of the box area. Evidently, there was no fluorescent signal detected in the superior temporal area where the dMRI-derived IFOF tract passes through (G).

The online version of this article includes the following figure supplement(s) for figure 7:

**Figure supplement 1.** Illustration of SLFIII by diffusion tractography and STP tomography (segmented out of the vIPFC-parietal projections).

*et al., 2018*). One major drawback of AAV vectors is the limited packaging capacity. AAVs usually deliver gene cassettes of approximately 4.8 Kb (i.e. one or two small genes) (*Nassi et al., 2015*), which has motivated us in pursuit of biocompatible nano-based carriers (*Cui et al., 2019*). It is well known that different AAV serotypes have their own sequences in the inverted terminal repeats such that they have distinct transfection bases toward various cell types in the brain. The recombinant virus we used was AAV2/9 which contains the inverted terminal repeats from AAV serotype 2 and the capsid proteins from AAV serotype 9. Previous studies have shown that AAV2 is the most widely used AAV vector and effectively transfects neurons of nonhuman primates (*Watakabe et al., 2015*). In a recent report on a mouse model, researchers co-injected AAV and a classical anterograde tracer - biotinylated dextran amine (BDA) into one brain region and observed long-range projections with similar patterns by both tracers, except that BDA had more retrograde-labeled neurons, probably uptaken by passing fibers in some areas (*Oh et al., 2014*). Together, our results have demonstrated that AAV2/9 vector was more suitable for long-range axonal fiber tracing, while VSV-ΔG was suitable for rapid gene expression and lentivirus for long-term gene expression in macaques.

### Comparison of STP tomography with diffusion tractography

Pioneering studies on cross-modality comparison across the whole-brain scale have been done by constructing a connectivity matrix using dMRI-based tractography and tracer-injection tracing in mice (*Calabrese et al., 2015*) and in monkeys (*Donahue et al., 2016; Girard et al., 2020; van den Heuvel et al., 2015*). The spatial correspondence of axonal fibers derived from diffusion tractography and GFP-labeled fluorescent images have been compared both in mice (*Harsan et al., 2013; Chen et al., 2015; Chang et al., 2017*) and in macaques (*Dauguet et al., 2007*). Dauguet and coworkers found that the somatosensory and motor tracts derived from diffusion tractography were visually in good agreement with the reconstructed 3D histological sections labeled by anterograde WGA-HRP tracer in a monkey brain, but suffered certain limitations for regions at remote locations from seeds (*Dauguet et al., 2007*). Moreover, the structural connectivity analyses based on the histological dataset provided varying correlative evidence between these two measurements (like  $r = 0.21$  *van den Heuvel et al., 2015* using the CoCoMac tracer data *Stephan, 2013* and  $r = 0.59$  *Donahue et al., 2016* using the tracer connectivity matrix from *Markov et al., 2014*). Note that such structural connectivity analysis does not describe a 3D correspondence of the axonal fiber trajectory, but an 'end-to-end' match. STP tomography effectively transformed a series of histological slice images into a 3D space with which dMRI-derived tracts were co-registered, thus enabling a direct, quantitative comparison of the high-throughput data from these two modalities. This is technically challenging due to a giant difference in scale between the axonal fibers and image resolution of dMRI (*Glasser et al., 2016*). We have taken meticulous steps to maximize the signal-to-noise ratio like using Gd-DTPA as an enhanced contrast agent (*D'Arceuil et al., 2007*) and to minimize the image artifacts in an ultrahigh field scanner for achieving a reasonably high spatial resolution. We observed that GFP-labeled axonal density maps not only significantly overlapped with dMRI-derived probabilistic maps throughout the traveling course but also demonstrated comparable connectivity strengths and patterns. But caution should be born in mind that diffusion tractography estimated the Brownian motion of water molecules, from which the directionality of axons cannot be distinguished (*Mori and Zhang, 2006*). The viral tracing data here contained only anterograde axonal fiber projections.

Our particular focus on the vIPFC connectivity profile leads us to clarify the existence of the IFOF in monkeys which is heavily debated (*Forkel et al., 2014*). The IFOF in human brain was first described in the early 20th century (*Curran, 1909*), whereby the anatomy of this pathway in human has been recently shown by micro-dissection and diffusion tractography studies (*Hau et al., 2016; Takemura et al., 2017*). Its entire course through the ventral part of the external capsule (EC) connects the occipital cortex and

the parietal and temporal cortices to the frontal cortex (*Sarubbo et al., 2019*). Some axonal tracing studies showed connections between frontal and occipital lobes in monkeys (*Gerbella et al., 2010; Markov et al., 2014*), which was consistent with the observation by tractography (*Feng et al., 2017*) and blunt dissection (*Sarubbo et al., 2019*) experiments. By contrast, other studies that are capable of tracking monosynaptic pathways failed (*Petrides, 2013*). Using the same ROIs seeds as prior studies (*Barrett et al., 2020; Feng et al., 2017*), our ex-vivo tractography did show fiber connections between frontal and occipital lobes in monkeys, matching the trajectory of IFOF in humans. By contrast, using anterograde AAV vector without trans-synaptic capability, we found that vIPFC fiber projections passed through external capsule, claustrum, and extreme capsule and anchored to the middle superior temporal region. Although the trajectory of vIPFC between frontal and temporal regions matched well with the diffusion tractography of IFOF, axonal projections of vIPFC never reached the occipital lobe. Lack of monosynaptic tracing data in human subjects, we could not rule out the possibility of same scenario for IFOF in humans. If the IFOF connects the frontal lobe with the occipital lobe in a trans-synaptic manner, it unveils a hitherto unknown information relay/integration process occurring in superior temporal area of the primate species which holds great implications for neural network computation. Nevertheless, unlike the direct monosynaptic connections reported between subdivisions of PFC such as OFC and the visual cortex in mice (*Zingg et al., 2014; Liu et al., 2020*), our results underscore a nontrivial species difference and raise interesting questions about the long-range brain organization and the functional role of superior temporal area in primates which definitely merits future examination.

In summary, we present a detailed excitatory connectivity projection map from vIPFC to the entire macaque brain, and demonstrate a broadly applicable roadmap of integrating 3D STP tomography labeled with antero-/retro-grade tracer and diffusion tractography for the mesoscopic mapping of brain circuits in the primate species.

## Materials and methods

### Key resources table

Reagent type (species) or resource	Designation	Source or reference	Identifiers	Additional information
Antibody	anti-CaMKIIa (Rabbit polyclonal)	Abcam	Cat# ab5683, RRID: <a href="#">AB_305050</a>	IF(1: 200)
Antibody	anti-GABA (Rabbit polyclonal)	Abcam	Cat# ab8891, RRID: <a href="#">AB_306844</a>	IF(1: 200)
Antibody	anti- NeuN (Mouse Monoclonal)	Millipore	Cat# MAB377, RRID: <a href="#">AB_2298772</a>	IF(1: 500)
Antibody	anti- GFP (Rabbit polyclonal)	Thermo Fisher Scientific	Cat# A-11122, RRID: <a href="#">AB_221569</a>	IF(1: 300)
Antibody	anti- GFAP (Rabbit polyclonal)	Boster (PMID: <a href="#">31101714</a> )	Cat# PB0046	IF(1: 200)
Antibody	Goat anti-Rabbit IgG (H + L) Alexa Fluor 405 (Goat polyclonal)	Thermo Fisher Scientific	Cat# A31556, RRID: <a href="#">AB_221605</a>	IF(1: 500)
Antibody	Donkey anti-Rabbit IgG (H + L) Alexa Fluor 568 (Donkey polyclonal)	Thermo Fisher Scientific	Cat# A10042, RRID: <a href="#">AB_2534017</a>	IF(1: 600)
Antibody	Goat anti-Mouse IgG (H + L) Alexa Fluor 568 (Goat polyclonal)	Thermo Fisher Scientific	Cat# A11031, RRID: <a href="#">AB_144696</a>	IF(1: 600)
Antibody	Goat anti-Mouse IgG (H + L) Alexa Fluor Plus 647 (Goat Polyclonal)	Thermo Fisher Scientific	Cat# A32728, RRID: <a href="#">AB_2633277</a>	IF(1: 500)
Antibody	Goat anti-Rabbit IgG (H + L) Alexa Fluor 488 (Goat Polyclonal)	Thermo Fisher Scientific	Cat# A11034, RRID: <a href="#">AB_2576217</a>	IF(1: 300)
Software, algorithm	Fiji (ImageJ) software	NIH	RRID: <a href="#">SCR_002285</a>	<a href="http://fiji.sc">http://fiji.sc</a>
Software, algorithm	MATLAB	Mathworks	RRID: <a href="#">SCR_001622</a>	<a href="https://www.mathworks.com/">https://www.mathworks.com/</a>
Software, algorithm	FSL software	University of Oxford	RRID: <a href="#">SCR_002823</a>	<a href="http://www.fmrib.ox.ac.uk/fsl">http://www.fmrib.ox.ac.uk/fsl</a>
Software, algorithm	ANTS - Advanced Normalization Tools	University of Pennsylvania	RRID: <a href="#">SCR_004757</a>	<a href="http://www.picml.upenn.edu/ANTS/">http://www.picml.upenn.edu/ANTS/</a>

### Animals and ethics statement

All experimental procedures for nonhuman primate research in this study were approved by the Animal Care Committee of Shanghai Institutes for Biological Sciences, Chinese Academy of Sciences, and conformed to the National Institutes of Health guidelines for the humane care and use of laboratory



**Table 1.** Injection cases and viral vectors used in this study.

ID	Species	Injection site	Viral vector	Expression time
#1	Macaca mulatta (M)	Cortex MD	VSV-ΔG-Tau-GFP VSV-ΔG-Tau-GFP	~5 d ~5 d
#2	Macaca mulatta (M)	Cortex MD	VSV-ΔG-Tau-GFP VSV-ΔG-Tau-GFP	~30 d ~90 d
#3	Macaca fascicularis (M)	Cortex Cortex Cortex MD	AAV2/9-CaMKIIα-Tau-GFP AAV2/9-hSyn-mCherry Lenti-UbC-GFP Lenti-UbC-GFP	~45 d ~45 d ~260 d ~260 d
#4	Macaca fascicularis (M)	MD	AAV2/9-CaMKIIα-Tau-GFP	~60 d
#5	Macaca fascicularis (M)	MD	AAV2/9-CaMKIIα-Tau-GFP	~60 d
#6	Macaca fascicularis (F)	MD	AAV2/9-CaMKIIα-Tau-GFP	~60 d
#7	Macaca fascicularis (M)	vIPFC	AAV2/9-CaMKIIα-Tau-GFP	~75 d
#8	Macaca fascicularis (F)	vIPFC	AAV2/9-CaMKIIα-Tau-GFP	~75 d
#9	Macaca fascicularis (F)	vIPFC	AAV2/9-CaMKIIα-Tau-GFP	~110 d
#10	Macaca fascicularis (F)	\	\	\

Abbreviations: M, male; F, female. MD, mediodorsal thalamus; vIPFC, ventrolateral prefrontal cortex; UbC, human ubiquitin C; hSyn, human synapsin I; CaMKII, Ca2+/calmodulin dependent protein kinase II; d, day.

animals. From November 2015 till November 2020, ten adult macaque monkeys (*Macaca mulatta* and *Macaca fascicularis*) weighting 3.5–12.2 kg ( $6.94 \pm 2.98$  kg) were used for in this study (**Table 1**), two of which (*Macaca fascicularis*) were used for ex-vivo ultrahigh field dMRI scanning.

### Viral vectors

Four viral vectors, including VSV-ΔG (VSV-ΔG-Tau-GFP, titer:  $5.0 \times 10^8$  PFU/mL), lentivirus (lentivirus-UbC-GFP, titer:  $1.33 \times 10^9$  TU/mL), and two constructs of AAV2/9 (AAV2/9-CaMKIIα-Tau-GFP, titer:  $8.47 \times 10^{13}$  vg/mL; AAV2/9-hSyn-mCherry, titer:  $1.6 \times 10^{13}$  vg/mL), were tested in this study (**Table 1**). AAV2/9 and VSV-ΔG were purchased from BrainVTA technology Co., Ltd. (Wuhan, China), and lentivirus was provided by a coauthor Z.Q's laboratory. Here, the recombinant AAV2/9 contained either a hSyn or CaMKIIα promoter to regulate the expression of either reporter gene mCherry in all neurons or fused Tau-GFP protein in glutamatergic excitatory neurons, respectively. Regarding the VSV vector, G protein was deleted to prevent transsynaptic spread. The last tested viral vector, Ubic promoter-driven lentivirus, expressed GFP in all eukaryotic cells.

### MRI-Guided Virus Injection

To precisely target brain regions in individual subjects, we performed in-vivo MRI scanning in monkeys and then used MRI images to guide the virus injection. T1 weighted images for each monkey were obtained with a 3T scanner (Siemens Tim Trio, Erlangen, Germany) under general anesthesia. A detailed description of in-vivo MRI scanning procedure has been described in our previous studies (*Cai et al., 2020; Zhan et al., 2021; Wang et al., 2013; Lv et al., 2021; Lv et al., 2016; Zhang et al., 2019*) and briefly summarized here. Anesthesia was induced by intramuscular injection of ketamine (10 mg per kg). Deep anesthesia was maintained by isoflurane (1.5–3%) and vital physiological signals were continuously monitored during MRI scanning. Anatomical scans were acquired with an MPRAGE sequence using the following parameters: TR = 2300ms, TE = 2.8ms, TI = 1100ms, spatial resolution 0.5 mm isotropic. The target regions were localized in each animal by warping the 3D digital atlas of Saleem and Logothetis (*Reveley et al., 2017*) to the individual T1 image using a symmetric normalization (SyN) algorithm. The location of the vIPFC was then calculated with regard to the stereotaxic space.

All procedures for virus injection were performed in strict aseptic conditions. The head of the animal was fixed in a stereotaxic apparatus, within the same coordinate space as the MRI images. The target area was then labeled and an incision was made to expose the skull. A burr hole with a 2 mm radius was drilled above the target according to the calculated coordinates, and the dura was carefully

incised to expose the cortical surface. The viral vector was delivered into the cortex using a 33-gauge Hamilton syringe controlled by an UltraMicroPump and a micro4 controller (WPI). The injection speed started with 200 nl/min and was increased to 400 nl/min; total injection volume was 10–20  $\mu$ l. After injection, the needle was retained for at least 15 min and drawn back at a rate of  $\sim$ 1 mm/min. The burr hole was then filled with bone wax and the skin was sutured. Cephalosporin was given for three consecutive days after surgery (25 mg/kg/day, i.m., once a day).

## Cryo-Sectioning

According to the expression time of individual virus (**Table 1**), animals were deeply anesthetized, and then transcardially perfused with 0.9% NaCl (pH = 7.2) followed by ice-cold 4% paraformaldehyde in 0.01 M phosphate buffered saline. Brains were extracted and post-fixed in 4% PFA for 3 days. Cryo-sectioning combined with wide field microscope imaging and confocal laser microscope imaging was performed for virus testing. The fixed brain was first cut into a block, then equilibrated sequentially in 15 and 30% sucrose in PBS until it sank to the bottom of the container. A cryostat microtome (Leica CM1950) was used to serially slice the brain into 50  $\mu$ m sections. Brain slices were preserved in a cryoprotectant solution (containing 30% ethanediol, 30% sucrose in PBS solution, pH = 7.2) for further immunofluorescence staining and imaging.

## Serial Two-Photon Tomography

Fluorescence signals of AAV labeled areas were detected and recorded using a customized STP tomography (**Figure 1—figure supplement 1**). To image the monkey brain, we customized the STP tomography system which was integrated a two-photon microscope (Bruker) with a vibratome (WPI) (**Figure 1—figure supplement 1**), computer controlled and fully automated. The XY stage covered a 50\*60 mm<sup>2</sup> area, and the 3D scanning of Z-volume stacks was achieved with using a stepper motor (Thorlabs) that traveled over 70 mm. The fixed brain that was embedded with 4% agarose was scanned in a 3T MRI to obtain ex-vivo T1 images. Using these T1 images as reference, the active imaged region of each section was determined during STP tomography for improved imaging efficiency. The embedded brain was then held via a magnetic adaptor to a stepper motor and immersed in a cutting bath filled with PBS containing 0.1% sodium azide. The vibratome blade was aligned in parallel with the leading edge of the specimen block. Brain images were captured from the anterior PFC to posterior V1 in the coronal plane. Fluorescence signals for the green channel (excitation wavelength light in 920 nm) and red channel (excitation wavelength light in 1045 nm) were acquired at 30  $\mu$ m below the cutting surface through a Nikon 16 x Water objective (N.A. = 0.8).

During serial scanning, the STP tomography system was fully automated: each optical section was imaged as a mosaic of fields of view on the block surface as the xy stage moved the brain under the objective; once an entire section was imaged, the xy stage moved the brain to the vibratome and cut off a 200  $\mu$ m section from the top of the sample. The remaining specimen was then moved back under the objective for imaging the next neighboring plane. Optical and mechanical sectioning were repeated until the complete brain data was collected. Hence fluorescent images of the whole monkey brain were continuously acquired (**Figure 1—figure supplement 2**).

High x-y resolution (0.95  $\mu$ m/pixel) serial 2D images were acquired in the coronal plane at a z-interval of 200  $\mu$ m across the entire macaque brain. The scanning time of a single field-of-view which contains 1,024 by 1,024 pixels was 1.629 s (i.e. pixel residence time was  $\sim$ 1.6  $\mu$ s), as resulted in a continuous  $\sim$ 1 month scanning and  $\sim$ 5 TB STP tomography data for a single monkey brain (**Figure 1—figure supplement 2**). Once finished scanning, all sections were retrieved from the cutting bath and stored in cryo protection solution (containing 30% glycol, 30% sucrose in PBS) at  $-20^{\circ}$ C for further histological examination. Three samples were injected with AAV in vIPFC, and two of them were able to be imaged with STP tomography. Unfortunately, one sample became 'loose' and fell off from the agar block after several weeks of imaging. So, the quantitative results were not shown in **Figure 3**.

## Histological staining

To perform immunofluorescence procedure, brain slices were incubated in blocking solution containing 5% BSA and 0.3% Triton X-100 in PBS at room temperature for 2 hr and then overnight with primary antibodies in PBS containing 3% BSA and 0.3% Triton X-100 at 4  $^{\circ}$ C. Slices were rinsed in PBS followed by Alexa Fluor-conjugated secondary antibodies at room temperature for 3 hr, and DAPI

(Cell signaling Cat# 4083 s) for 30 min at room temperature. The following primary antibodies were used: CaMKIIa (1:200, Abcam, Cat# ab5683, RRID: [AB\\_305050](#)), GABA (1:200, Abcam Cat# ab8891, RRID: [AB\\_306844](#)), NeuN (1:500, Millipore, Cat# MAB377, RRID: [AB\\_2298772](#)), GFP (1:300, Thermo Fisher Scientific, Cat# A-11122, RRID: [AB\\_221569](#)), GFAP (1:200, Boster, Cat# PB0046). The following secondary antibodies were used: Goat anti-Rabbit IgG (H + L) Alexa Fluor 405 (1:500, Thermo Fisher Scientific, Cat# A31556, RRID: [AB\\_221605](#)), Donkey anti-Rabbit IgG (H + L) Alexa Fluor 568 (1:600, Thermo Fisher Scientific, Cat# A10042, RRID: [AB\\_2534017](#)), Goat anti-Mouse IgG (H + L) Alexa Fluor 568 (1:600, Thermo Fisher Scientific, Cat# A11031, RRID: [AB\\_144696](#)), Goat anti-Mouse IgG (H + L) Alexa Fluor Plus 647 (1:500, Thermo Fisher Scientific, Cat# A32728, RRID: [AB\\_2633277](#)), Goat anti-Rabbit IgG (H + L) Alexa Fluor 488 (1:300, Thermo Fisher Scientific, Cat# A11034, RRID: [AB\\_2576217](#)). The brain slices were mounted onto customized 2 × 3 inch or 3 × 4 inch glass slides. The sections were then scanned using an Olympus VS120 (Olympus, Japan), a wide field microscope, with a U Plan Super Apo 10 × objective (N.A. = 0.4) at a resolution of 0.65 μm/pixel. High resolution fluorescent images were acquired with a confocal laser microscope Nikon TiE (Nikon, Tokyo, Japan) with a Plan Fluo 40 × Oil DIC N2 objective (N.A. = 1.3), 0.5 μm Z-interval, and 1024 × 1,024 pixels.

## Fluorescence image preprocessing

Fluorescent images of the macaque brain usually contain strong autofluorescence signal (**Figure 1—figure supplement 3A-E**), mainly caused by the accumulation of lipofuscin (**Economo et al., 2016**). Autofluorescence provides good contrast between gray matter and white matter, which is rather useful for image registration. But the presence of autofluorescence is undesirable for the axon tracing procedure since this background signal sometimes is much stronger than that of some thin GFP labeled axons (**Figure 1—figure supplement 3A-E**). Nevertheless, thanks to the broad emission spectrum of lipofuscin (**Hunnicutt et al., 2016**), autofluorescence and GFP signals are easily distinguishable from each other. We therefore implemented and compared the following three methods for background reduction: (1) transforming the GFP signal from the green channel (488 nm) to the blue channel (405 nm) using immunofluorescent staining (**Figure 1—figure supplement 3M**), (2) subtracting the normalized autofluorescence signal in the red channel from the green channel (**Figure 1—figure supplement 3F**), which contains both GFP signal and autofluorescence background signal, (3) supervised machine learning for autofluorescence exclusion (**Figure 1—figure supplement 3J**).

The first method involved staining the brain tissue with anti-GFP antibody and Alexa Fluor 405 conjugated secondary antibody to transform the GFP signal from a green channel to a blue channel. Unlike the green and red channels, the transferred blue channel (**Figure 1—figure supplement 3M**) did not contain high-intensity autofluorescence puncta. Although this post-hoc thick-section immunofluorescent method successfully reduced autofluorescence, it was incompatible with the block face imaging method. The second one was to subtract the normalized red channel from the green channel using the broad emission spectrum characteristic of autofluorescence puncta, which was able to remove high intensity background signal (**Figure 1—figure supplement 3F**). The third was based on a supervised machine learning plugin for ImageJ, trainable WEKA segmentation (**Arganda-Carreras et al., 2017**), which classifies and binarizes GFP and autofluorescence background signal for background exclusion (**Figure 1—figure supplement 3J**). Both subtraction and machine learning methods were used for better visualization of fluorescence images when necessary, whereas only the supervised machine learning approach was used for quantitative analysis of STP data (**Hunnicutt et al., 2016**).

## STP Image Processing

STP tomography data processing included axonal fiber detection, image stitching, down sampling, cross-modality registration and quantification. The data analysis was undertaken on a compute cluster with a 3.1–3.3 GHz 248 core CPU, 2.8T of RAM, and 17472 CUDA cores. Fluorescent images of primate (**Abe et al., 2017**) brain often contain high-intensity dot-looking background signal caused by accumulation of lipofuscin. Thanks to the broad emission spectrum of lipofuscin, dot-looking background and GFP-positive axonal varicosities are easily distinguishable from each other. For instance (**Figure 1—figure supplement 4**), axonal varicosities can be selectively excited in green channel, while dot-looking background lipofuscin usually present in both green channel and red channel. During quantitative analysis, a machine learning algorithm was adopted to reliably segment the GFP labeled axonal fibers including axonal varicosities, and remove the lipofuscin background (**Arganda-Carreras**

*et al., 2017; Gehrlach et al., 2020*). The total computational time for the machine learning predictions in one macaque brain was ~1.5 months. To evaluate overall classifier performance, the precision–recall F measure, also called F-score, was computed by using additional four labeled images as test sets. Higher accuracy performance achieved by the classifier often yield higher F-scores ( $94.41 \pm 1.99\%$ , mean  $\pm$  S.E.M.). During STP tomography scanning, each field of view (FOV) was saved as a  $1024 \times 1024$ -pixel image. For image stitching, individual FOV images from red channel, green channel and segmented GFP signal were stitched into full tissue sections using the Terastitcher software. A convolutional neural network-based denoising approach was used to improve SNR of images when necessary (*Krull et al., 2019*). The natural alignment of serial images generated by STP tomography allowed to stack the section images to form a coherent reconstructed 3D volume (*Ragan et al., 2012*). In order to localize the virus injection site, a threshold was set at green channel to retain the fluorescence signal only from the cell soma for each section image. Images of the red channel and injection site volumes were downsampled to a resolution of  $200 \times 200 \times 200$   $\mu\text{m}$  grid. For serial segmented GFP images, the total signal intensity was computed for each  $200 \times 200$   $\mu\text{m}$  grid by summing the number of signal-positive pixels in that voxel. Red channel volume was used to perform registration to the monkey brain template, as red channel images contain visible anatomical information of brain structures (*Kuan et al., 2015*). The brain template of cynomolgus macaque was adopted from an MRI-based atlas generated from 162 cynomolgus monkeys (*Lv et al., 2021*). We warped the red channel volume to the template space by using a symmetric normalization (SyN) algorithm in ANTs (*Figure 1—figure supplement 5*). For registration to the 3D common space, it took half an hour approximately. The cortical label was adopted from the D99 parcellation map (*Reveley et al., 2017*), and subcortical label was adopted from INIA19 parcellation map (*Rohlfing et al., 2012*). Also the segmented GFP volume and injection site volume were co-registered onto the same template. Density of GFP signal and total GFP volume in each parcellated brain region were used to represent the axonal connectivity strength. Percent of total projection was defined by the GFP-positive pixel count within each parcellated brain region (or brain lobe) normalized to the total of all GFP-positive pixels. Additionally, the percent innervation density was calculated as the proportion of density of GFP pixel counts covering the maximal density of GFP pixel counts of the brain. To create plots that display the data along the anterior-posterior axis (e.g. % density innervation), the location of ear bar zero was used as the origin. The percent innervation density of each cortical region innervated by vIPFC was rendered onto a brain surface. *Figures 3–4* and *Figure 4—figure supplements 2–4* were derived from sample #8 with infected area in 45, 12 I and 44 of vIPFC. *Figure 1—figure supplement 6* was derived from sample #7 with infected area in 12 I and 45 of vIPFC.

## Ex-Vivo MRI Scanning and Data Preprocessing

We collected dMRI data using an 11.7T horizontal MRI system (Bruker Biospec 117/16 USR, Ettlingen, Germany), equipped with a 72 mm volume resonator and an actively shielded, high performance BGA-S series gradient system (gradient strength: 740 mT/m, slew rate: 6660 T/m/s). After a fixation period of ~30 days, the whole brain specimen was immersed in a 1:100 dilution of a 1 mmol/mL gadolinium MR contrast agent (Magnevist, Bayer Pharma AG, Germany) mixed with phosphate buffered saline (PBS) solution for 14 days. Before MRI scanning, the specimen was washed and drained of water from the surface, then positioned into a customized container which was 3D printed for perfect accommodation of the brain sample. Thus the brain was held steadily during MRI scanning. And the container was filled with FOMBLIN perfluoropolyether (Solvay Solexis Inc Thorofare, NJ, USA) for susceptibility matching and improved magnetic field homogeneity. The specimen was degassed with a vacuum pump for 24 h under 0.1 atmosphere pressure to remove all air bubbles in the sample at 20 °C (magnet room temperature). The ex-vivo macaque brain was scanned on a 11.7T animal MRI system (Bruker Biospec 117/16 USR, Ettlingen, Germany), equipped with a 72 mm volume resonator and an actively shielded, high performance BGA-S series gradient system (gradient strength: 740 mT/m, slew rate: 6660 T/m/s). dMRI images were acquired using a 3D diffusion-weighted spin echo pulse sequence with single-line read-out, TR/TE = 82/22.19ms, FOV =  $64 \times 54$  mm, matrix =  $128 \times 108$ , slice thickness = 0.5 mm and averages = 3, which included 60 diffusion directions with  $b = 4000$   $\text{s}/\text{mm}^2$  ( $\Delta/\delta = 15/2.8$ ms, maximum  $b$  value = 4234.97, gradient amplitude = 97.19 mT/m) and five nondiffusion encoding ( $b = 0$   $\text{s}/\text{mm}^2$ ) directions. For the ex-vivo diffusion MRI data acquisition, the  $b$ -value was recommended to set at 4000  $\text{s}/\text{mm}^2$  (*D’Arceuil et al., 2007; Dyrby et al., 2011*). T2

weighted images were acquired using a 2D Turbo RARE sequence with TR/TE = 8353.42/28.8ms, flip angle = 87°, matrix = 450 × 450, FOV = 54 × 45 mm, slice thickness = 0.5 mm, and averages = 6. T1 weighted images were acquired using 3D FLASH sequence with TR/TE = 40/5.5ms, flip angle = 15°, matrix = 290 × 225, FOV = 58 × 45 mm, slice thickness = 0.2 mm, and averages = 4. All scanning was performed at room temperature (approximately 20 °C) and the total scan time was approximately 36 hr.

Visual inspection of MRI data was first performed to ensure that there were no obvious image artifacts and geometric distortions. Then we calculated the signal-to-noise ratio (SNR) for typical diffusion images. As diffusion images were acquired by spin warp imaging (image reconstruction by a 3D Fourier transform) with a volume quadrature coil, the SNRs were calculated using the 'two-region' approach (Dietrich et al., 2007; Kaufman et al., 1989). Specifically, for each gradient encoding direction, the deep white matter (WM) were extracted in subject-native diffusion space to represent the signal (Sijbers et al., 1998); a region positioned in the no signal area at the corner of the image was used to represent the noise. As a rule of thumb, the SNR of  $b = 0$  s/mm<sup>2</sup> images should be minimally larger than 20 for obtaining relatively unbiased measures of parameters such as FA (Mukherjee et al., 2008). Typical SNRs of diffusion images with  $b = 0$  and  $b = 4000$  in the present study were  $48.34 \pm 8.50$  and  $23.13 \pm 2.05$ , respectively. It allowed a reliable seed-based 3D reconstruction for diffusion tractography, as illustrated in Figure 5. The dMRI data was preprocessed using the FSL software (<http://www.fmrib.ox.ac.uk/fsl>) (Behrens et al., 2007). Individual image volumes were co-registered with  $b = 0$  images to account for eddy currents and B0 drift using affine registration in FLIRT (Jenkinson and Smith, 2001). A custom in-house script was applied to reorient the corresponding gradient direction matrix. Careful steps have been taken to minimize artifacts caused by motion and field distortion, and image correction was applied only if necessary (Andersson and Sotiropoulos, 2016; Andersson and Sotiropoulos, 2015).

## Reconstruction and comparison of diffusion tractography and axonal tracing

We first identified the injection-site volume in the vIPFC in STP tomography data, warped it to the space of dMRI volume and used it as a seed mask for tractography. Then the injection site related tractography was constructed using the preprocessed dMRI images in FSL toolbox. BEDPOSTX was used for Bayesian estimation of a crossing fiber model with three-fiber orientation structure for each voxel using Markov chain-Monte Carlo sampling (Behrens et al., 2007). This provided a voxel-wise estimate of the angular distribution of local tract direction for each fiber, which was a starting point for tractography. Tractography was then performed from the injection-site seed masks without waypoint mask and termination mask using the Probtrackx probabilistic tractography software (Behrens et al., 2007). A probabilistic map of fiber tracts was generated with 500  $\mu$ m isotropic resolution. A probabilistic map provided, at each voxel, a connectivity value, corresponding to the total number of samples that passed from the seed region through that voxel. The following settings were used: number of samples per voxel = 5000, number of steps per sample = 2000, step length = 0.2 mm, loop check, default curvature threshold = 0.2 (corresponding to a minimum angle of approximately  $\pm 80$  degrees), subsidiary fiber volume threshold = 0.01, seed sphere sampling = 0 and no way-point or termination mask. In the resulting map, each voxel's value represented the degree of connectivity between it and the seed voxels. To generate dMRI-derived fiber tracts, the resulting probabilistic maps were set at a threshold, i.e., any voxel below threshold was set to zero. In parallel, segmented fluorescence images from the STP tomography data were downsampled to 500  $\mu$ m grid to generate axonal density maps. The signal intensity of an axonal density map was computed for each 500 × 500  $\mu$ m<sup>2</sup> grid by summing the number of GFP-positive pixels within that area. Note that the axonal density map was also filtered by setting an intensity threshold of  $10^{2.8}$  to minimize false positives due to segmentation artefacts (Oh et al., 2014). After co-registered the probabilistic maps and the axonal density maps onto the same template, both Dice coefficients and pixel-wise Pearson coefficients were calculated to quantitatively assess the spatial overlap (Dice, 1945; Crum et al., 2006).

As described recently (Barrett et al., 2020), the inferior fronto-occipital fasciculus was reconstructed using streamline-based probabilistic tractography. We ran this probabilistic tractography tool in MRTrix3 (<https://www.mrtrix.org/>) via bootstrapping (Jones, 2008). Streamlines were seeded over the whole brain area that encapsulated the tract of interest. Two inclusion masks were used to define

two regions that each tract must pass through, and only streamlines that pass through both regions are retained. One exclusion mask was used to restrict tracking to the contralateral hemisphere of the brain. The inclusion and exclusion masks were drawn manually as described previously ([Barrett et al., 2020](#)): the first mask was placed on the anterior border of the occipital lobe in the coronal view, the second mask was placed on the external/extreme capsules in the coronal view, and the third mask was cover the whole left hemisphere as the exclusion mask. The delineation process was performed using the MRlcro (<https://crnl.readthedocs.io/>) software. Using this ‘waypoint’ method, the resultant streamlines were able to meet our preset conditions. To further reduce false positive tracts, any streamlines that were identified as either attached to other tracts or anatomically implausible trajectories were manually removed.

According to previous studies ([Sani et al., 2019](#); [de Schotten et al., 2011](#)), two inclusion ROIs and two exclusion ROIs were used for reconstructing the SLFIII in diffusion tractography. Two inclusion regions were placed in the frontal and parietal lobes (violet and red areas marked in [Figure 7—figure supplement 1A](#)). Two exclusion regions were placed in the temporal and occipital lobes, respectively.

Details of streamline-based probabilistic tractography processing were described here. The fiber orientation distribution function (FOD) was estimated with MRtrix3 (<https://www.mrtrix.org/>) ([Tournier et al., 2012](#)) using the *tournier* algorithm for single-tissue Constrained spherical deconvolution [Tournier et al., 2013](#). For fiber tracking, we then used *tckgen* with the *Tensor\_Prob* tracking algorithm in MRtrix3 ([Jones, 2008](#)). Within each image voxel, a residual bootstrap was performed to obtain a unique realization of the dMRI data in that voxel for each streamline. These data are then sampled via trilinear interpolation at each streamline step, the diffusion tensor model is fitted, and the streamline follows the orientation of the principal eigenvector of that tensor. The following additional *tckgen* settings and inputs were used: step size of 0.25 mm, max. angle between successive steps = 45°, max. length = 150 mm, min. length value set the min. length 10 mm, cutoff FA value = 0.1, b-vectors and b-values from the diffusion-weighted gradient scheme in the FSL format, b-value scaling mode = true, maximum number of fibers = 10,000, and unidirectional tracking.

For a direct comparison between diffusion-derived the IFOF tract and vIPFC projection fibers, we first generated the track density images of the IFOF tract and co-registered them onto the space of the template. The spatial overlap of GFP-positive vIPFC projection fibers and the IFOF tract were then detected with using ImageJ and FSL software in both 2D and 3D space ([Figure 7B](#)). The Szymkiewicz-Simpson overlap coefficient was adopted to quantify the spatial relationship between the IFOF tract and vIPFC projectome, which was defined as the size of the union of them over the size of the smaller set:

$$\text{overlap (IFOF, vIPFC)} = \frac{|IFOF \cap vIPFC|}{\min(|IFOF|, |vIPFC|)}$$

The Szymkiewicz-Simpson overlap coefficient ranges from 0 (no overlap) to 1 (if the IFOF tract is found in its entirety in vIPFC projectome).

## Materials availability

All the virus vectors used in this paper are available from the authors for sample test.

## Acknowledgements

We would like to thank Jinqiang Peng and Jie Xu for their assistance to data acquisition, and thank Drs. John Gore, Ed Callaway and Anna Roe for their stimulating discussions and suggestions during the preparation of this study. This work was supported by the Key-Area Research and Development Program of Guangdong Province (2019B030335001), National Natural Science Foundation (No. 82151303), National Key R&D Program of China (No. 2021ZD0204002), Shanghai Municipal Science and Technology Major Project (No. 2018SHZDZX05), the Strategic Priority Research Program of Chinese Academy of Science (No. XDB32000000), and Peking-Tsinghua Center for Life Sciences.

## Additional information

### Funding

Funder	Grant reference number	Author
Key-Area Research and Development Program of Guangdong Province	2019B030335001	Zheng Wang
National Key Research and Development Program of China	No. 2021ZD0204002	Zheng Wang
Chinese Academy of Sciences	Strategic Priority Research Program No. XDB32000000	Zheng Wang
National Natural Science Foundation of China	82151303	Zheng Wang
Shanghai Municipal Science and Technology Commission	Major Project No. 2018SHZDZX05	Zheng Wang
Peking-Tsinghua Center for Life Sciences		Zheng Wang

The funders had no role in study design, data collection and interpretation, or the decision to submit the work for publication.

### Author contributions

Mingchao Yan, Wenwen Yu, Data curation, Formal analysis, Investigation, Methodology, Writing – original draft; Qian Lv, Data curation, Formal analysis, Investigation, Methodology, Validation; Qiming Lv, Tingting Bo, Xiaoyu Chen, Yilin Liu, Yafeng Zhan, Shengyao Yan, Xiangyu Shen, Formal analysis, Investigation, Methodology; Baofeng Yang, Investigation, Methodology; Qiming Hu, Jiangli Yu, Data curation, Formal analysis, Methodology; Zilong Qiu, Yuanjing Feng, Xiao-Yong Zhang, He Wang, Conceptualization, Methodology, Resources; Fuqiang Xu, Conceptualization, Investigation, Methodology, Resources; Zheng Wang, Conceptualization, Funding acquisition, Investigation, Project administration, Supervision, Writing – review and editing

### Author ORCIDs

Tingting Bo <http://orcid.org/0000-0002-9080-5165>

Xiao-Yong Zhang <http://orcid.org/0000-0001-8965-1077>

He Wang <http://orcid.org/0000-0002-2053-9439>

Fuqiang Xu <http://orcid.org/0000-0002-4382-9797>

Zheng Wang <http://orcid.org/0000-0001-7138-8581>

### Ethics

All experimental procedures for nonhuman primate research in this study were approved by the Animal Care Committee of Shanghai Institutes for Biological Sciences, Chinese Academy of Sciences (ER-SIBS-221601P), and conformed to the National Institutes of Health guidelines for the humane care and use of laboratory animals.

### Decision letter and Author response

Decision letter <https://doi.org/10.7554/eLife.72534.sa1>

Author response <https://doi.org/10.7554/eLife.72534.sa2>

## Additional files

### Supplementary files

- Transparent reporting form

**Data availability**

There is no publicly accessible resource for hosting such big connectome data. Therefore we host it ourselves on an institutional FTP server which can be accessed via username and password (available upon request). We commit to keeping it available for at least 5 years, and provide alternative procedures where users can copy any or all of it to their own computer if needed.

**References**

- Abe H**, Tani T, Mashiko H, Kitamura N, Miyakawa N, Mimura K, Sakai K, Suzuki W, Kurotani T, Mizukami H, Watakabe A, Yamamori T, Ichinohe N. 2017. 3D reconstruction of brain section images for creating axonal projection maps in marmosets. *Journal of Neuroscience Methods* **286**:102–113. DOI: <https://doi.org/10.1016/j.jneumeth.2017.04.016>, PMID: 28577985
- Albanese A**, Chung K. 2016. Whole-brain imaging reaches new heights (and lengths). *eLife* **5**:e13367. DOI: <https://doi.org/10.7554/eLife.13367>, PMID: 26789654
- Amato SP**, Pan F, Schwartz J, Ragan TM. 2016. Whole Brain Imaging with Serial Two-Photon Tomography. *Frontiers in Neuroanatomy* **10**:31. DOI: <https://doi.org/10.3389/fnana.2016.00031>, PMID: 27047350
- Andersson JLR**, Sotiropoulos SN. 2015. Non-parametric representation and prediction of single- and multi-shell diffusion-weighted MRI data using Gaussian processes. *NeuroImage* **122**:166–176. DOI: <https://doi.org/10.1016/j.neuroimage.2015.07.067>, PMID: 26236030
- Andersson JLR**, Sotiropoulos SN. 2016. An integrated approach to correction for off-resonance effects and subject movement in diffusion MR imaging. *NeuroImage* **125**:1063–1078. DOI: <https://doi.org/10.1016/j.neuroimage.2015.10.019>, PMID: 26481672
- Arganda-Carreras I**, Kaynig V, Rueden C, Eliceiri KW, Schindelin J, Cardona A, Sebastian Seung H. 2017. Trainable Weka Segmentation: a machine learning tool for microscopy pixel classification. *Bioinformatics (Oxford, England)* **33**:2424–2426. DOI: <https://doi.org/10.1093/bioinformatics/btx180>, PMID: 28369169
- Bakker R**, Wachtler T, Diesmann M. 2012. CoCoMac 2.0 and the future of tract-tracing databases. *Frontiers in Neuroinformatics* **6**:30. DOI: <https://doi.org/10.3389/fninf.2012.00030>, PMID: 23293600
- Barrett RLC**, Dawson M, Dyrby TB, Ptito M, D’Arceuil H, Croxson PL, Johnson PJ, Howells H, Forkel SJ, Dell’Acqua F, Catani M. 2020. Differences in Frontal Network Anatomy Across Primate Species. *The Journal of Neuroscience* **40**:2094–2107. DOI: <https://doi.org/10.1523/JNEUROSCI.1650-18.2019>, PMID: 31949106
- Basser PJ**, Mattiello J, LeBihan D. 1994. MR diffusion tensor spectroscopy and imaging. *Biophysical Journal* **66**:259–267. DOI: [https://doi.org/10.1016/S0006-3495\(94\)80775-1](https://doi.org/10.1016/S0006-3495(94)80775-1), PMID: 8130344
- Bedbrook CN**, Deverman BE, Gradinaru V. 2018. Viral Strategies for Targeting the Central and Peripheral Nervous Systems. *Annual Review of Neuroscience* **41**:323–348. DOI: <https://doi.org/10.1146/annurev-neuro-080317-062048>, PMID: 29709207
- Behrens TEJ**, Berg HJ, Jbabdi S, Rushworth MFS, Woolrich MW. 2007. Probabilistic diffusion tractography with multiple fibre orientations: What can we gain? *NeuroImage* **34**:144–155. DOI: <https://doi.org/10.1016/j.neuroimage.2006.09.018>, PMID: 17070705
- Beier KT**, Saunders A, Oldenburg IA, Miyamichi K, Akhtar N, Luo L, Whelan SPJ, Sabatini B, Cepko CL. 2011. Anterograde or retrograde transsynaptic labeling of CNS neurons with vesicular stomatitis virus vectors. *PNAS* **108**:15414–15419. DOI: <https://doi.org/10.1073/pnas.1110854108>, PMID: 21825165
- Bienkowski MS**, Bowman I, Song MY, Gou L, Ard T, Cotter K, Zhu M, Benavidez NL, Yamashita S, Abu-Jaber J, Azam S, Lo D, Foster NN, Hintiryan H, Dong H-W. 2018. Integration of gene expression and brain-wide connectivity reveals the multiscale organization of mouse hippocampal networks. *Nature Neuroscience* **21**:1628–1643. DOI: <https://doi.org/10.1038/s41593-018-0241-y>, PMID: 30297807
- Borra E**, Gerbella M, Rozzi S, Luppino G. 2011. Anatomical evidence for the involvement of the macaque ventrolateral prefrontal area 12r in controlling goal-directed actions. *The Journal of Neuroscience* **31**:12351–12363. DOI: <https://doi.org/10.1523/JNEUROSCI.1745-11.2011>, PMID: 21865477
- Cai DC**, Wang Z, Bo T, Yan S, Liu Y, Liu Z, Zeljic K, Chen X, Zhan Y, Xu X, Du Y, Wang Y, Cang J, Wang GZ, Zhang J, Sun Q, Qiu Z, Ge S, Ye Z, Wang Z. 2020. MECP2 Duplication Causes Aberrant GABA Pathways, Circuits and Behaviors in Transgenic Monkeys: Neural Mappings to Patients with Autism. *The Journal of Neuroscience* **40**:3799–3814. DOI: <https://doi.org/10.1523/JNEUROSCI.2727-19.2020>, PMID: 32269107
- Calabrese E**, Badea A, Cofer G, Qi Y, Johnson GA. 2015. A Diffusion MRI Tractography Connectome of the Mouse Brain and Comparison with Neuronal Tracer Data. *Cerebral Cortex* **25**:4628–4637. DOI: <https://doi.org/10.1093/cercor/bhv121>, PMID: 26048951
- Carlén M**. 2017. What constitutes the prefrontal cortex? *Science (New York, N.Y.)* **358**:478–482. DOI: <https://doi.org/10.1126/science.aan8868>, PMID: 29074767
- Catani M**, Howard RJ, Pajevic S, Jones DK. 2002. Virtual in vivo interactive dissection of white matter fasciculi in the human brain. *NeuroImage* **17**:77–94. DOI: <https://doi.org/10.1006/nimg.2002.1136>, PMID: 12482069
- Chang EH**, Argyelan M, Aggarwal M, Chandon T-SS, Karlsgodt KH, Mori S, Malhotra AK. 2017. The role of myelination in measures of white matter integrity: Combination of diffusion tensor imaging and two-photon microscopy of CLARITY intact brains. *NeuroImage* **147**:253–261. DOI: <https://doi.org/10.1016/j.neuroimage.2016.11.068>, PMID: 27986605
- Chen H**, Liu T, Zhao Y, Zhang T, Li Y, Li M, Zhang H, Kuang H, Guo L, Tsien JZ, Liu T. 2015. Optimization of large-scale mouse brain connectome via joint evaluation of DTI and neuron tracing data. *NeuroImage* **115**:202–213. DOI: <https://doi.org/10.1016/j.neuroimage.2015.04.050>, PMID: 25953631



- Crum WR**, Camara O, Hill DLG. 2006. Generalized overlap measures for evaluation and validation in medical image analysis. *IEEE Transactions on Medical Imaging* **25**:1451–1461. DOI: <https://doi.org/10.1109/TMI.2006.880587>, PMID: 17117774
- Cui Y**, Li X, Zeljic K, Shan S, Qiu Z, Wang Z. 2019. Effect of PEGylated Magnetic PLGA-PEI Nanoparticles on Primary Hippocampal Neurons: Reduced Nanoneurotoxicity and Enhanced Transfection Efficiency with Magnetofection. *ACS Applied Materials & Interfaces* **11**:38190–38204. DOI: <https://doi.org/10.1021/acsami.9b15014>, PMID: 31550131
- Curran EJ**. 1909. A new association fiber tract in the cerebrum with remarks on the fiber tract dissection method of studying the brain. *Journal of Comparative Neurology and Psychology* **19**:645–656. DOI: <https://doi.org/10.1002/cne.920190603>
- Dauguet J**, Peled S, Berezovskii V, Delzescaux T, Warfield SK, Born R, Westin C-F. 2007. Comparison of fiber tracts derived from in-vivo DTI tractography with 3D histological neural tract tracer reconstruction on a macaque brain. *NeuroImage* **37**:530–538. DOI: <https://doi.org/10.1016/j.neuroimage.2007.04.067>, PMID: 17604650
- de Schotten MT**, Dell'Acqua F, Forkel SJ, Simmons A, Vergani F, Murphy DGM, Catani M. 2011. A lateralized brain network for visuospatial attention. *Nature Neuroscience* **14**:1245–1246. DOI: <https://doi.org/10.1038/nn.2905>, PMID: 21926985
- Dice LR**. 1945. Measures of the Amount of Ecologic Association Between Species. *Ecology* **26**:297–302. DOI: <https://doi.org/10.2307/1932409>
- Dietrich O**, Raya JG, Reeder SB, Reiser MF, Schoenberg SO. 2007. Measurement of signal-to-noise ratios in MR images: influence of multichannel coils, parallel imaging, and reconstruction filters. *Journal of Magnetic Resonance Imaging* **26**:375–385. DOI: <https://doi.org/10.1002/jmri.20969>, PMID: 17622966
- Donahue CJ**, Sotiropoulos SN, Jbabdi S, Hernandez-Fernandez M, Behrens TE, Dyrby TB, Coalson T, Kennedy H, Knoblauch K, Van Essen DC, Glasser MF. 2016. Using Diffusion Tractography to Predict Cortical Connection Strength and Distance: A Quantitative Comparison with Tracers in the Monkey. *The Journal of Neuroscience* **36**:6758–6770. DOI: <https://doi.org/10.1523/JNEUROSCI.0493-16.2016>, PMID: 27335406
- Dyrby TB**, Baaré WFC, Alexander DC, Jelsing J, Garde E, Søgaard LV. 2011. An ex vivo imaging pipeline for producing high-quality and high-resolution diffusion-weighted imaging datasets. *Human Brain Mapping* **32**:544–563. DOI: <https://doi.org/10.1002/hbm.21043>, PMID: 20945352
- Dyrby TB**, Innocenti GM, Bech M, Lundell H. 2018. Validation strategies for the interpretation of microstructure imaging using diffusion MRI. *NeuroImage* **182**:62–79. DOI: <https://doi.org/10.1016/j.neuroimage.2018.06.049>, PMID: 29920374
- D'Arceuil HE**, Westmoreland S, de Crespigny AJ. 2007. An approach to high resolution diffusion tensor imaging in fixed primate brain. *NeuroImage* **35**:553–565. DOI: <https://doi.org/10.1016/j.neuroimage.2006.12.028>, PMID: 17292630
- Economo MN**, Clack NG, Lavis LD, Gerfen CR, Svoboda K, Myers EW, Chandrashekar J. 2016. A platform for brain-wide imaging and reconstruction of individual neurons. *eLife* **5**:e10566. DOI: <https://doi.org/10.7554/eLife.10566>, PMID: 26796534
- Feng L**, Jeon T, Yu Q, Ouyang M, Peng Q, Mishra V, Pletikos M, Sestan N, Miller MI, Mori S, Hsiao S, Liu S, Huang H. 2017. Population-averaged macaque brain atlas with high-resolution ex vivo DTI integrated into in vivo space. *Brain Structure & Function* **222**:4131–4147. DOI: <https://doi.org/10.1007/s00429-017-1463-6>, PMID: 28634624
- Folloni D**, Sallet J, Khrapitchev AA, Sibson N, Verhagen L, Mars RB. 2019. Dichotomous organization of amygdala/temporal-prefrontal bundles in both humans and monkeys. *eLife* **8**:e47175. DOI: <https://doi.org/10.7554/eLife.47175>, PMID: 31689177
- Forkel SJ**, Thiebaut de Schotten M, Kawadler JM, Dell'Acqua F, Danek A, Catani M. 2014. The anatomy of fronto-occipital connections from early blunt dissections to contemporary tractography. *Cortex; a Journal Devoted to the Study of the Nervous System and Behavior* **56**:73–84. DOI: <https://doi.org/10.1016/j.cortex.2012.09.005>, PMID: 23137651
- Gehrlach DA**, Weiand C, Gaitanos TN, Cho E, Klein AS, Hennrich AA, Conzelmann K-K, Gogolla N. 2020. A whole-brain connectivity map of mouse insular cortex. *eLife* **9**:e55585. DOI: <https://doi.org/10.7554/eLife.55585>, PMID: 32940600
- Gerbella M**, Belmalih A, Borra E, Rozzi S, Luppino G. 2010. Cortical connections of the macaque caudal ventrolateral prefrontal areas 45A and 45B. *Cerebral Cortex (New York, N.Y)* **20**:141–168. DOI: <https://doi.org/10.1093/cercor/bhp087>, PMID: 19406905
- Girard G**, Caminiti R, Battaglia-Mayer A, St-Onge E, Ambrosen KS, Eskildsen SF, Krug K, Dyrby TB, Descoteaux M, Thiran JP, Innocenti GM. 2020. On the cortical connectivity in the macaque brain: A comparison of diffusion tractography and histological tracing data. *NeuroImage* **221**:117201. DOI: <https://doi.org/10.1016/j.neuroimage.2020.117201>, PMID: 32739552
- Glasser MF**, Smith SM, Marcus DS, Andersson JLR, Auerbach EJ, Behrens TEJ, Coalson TS, Harms MP, Jenkinson M, Moeller S, Robinson EC, Sotiropoulos SN, Xu J, Yacoub E, Ugurbil K, Van Essen DC. 2016. The Human Connectome Project's neuroimaging approach. *Nature Neuroscience* **19**:1175–1187. DOI: <https://doi.org/10.1038/nn.4361>, PMID: 27571196
- Haber SN**, Tang W, Choi EY, Yendiki A, Liu H, Jbabdi S, Versace A, Phillips M. 2020. Circuits, Networks, and Neuropsychiatric Disease: Transitioning From Anatomy to Imaging. *Biological Psychiatry* **87**:318–327. DOI: <https://doi.org/10.1016/j.biopsych.2019.10.024>, PMID: 31870495

- Han X, Qian X, Bernstein JG, Zhou H-H, Franzesi GT, Stern P, Bronson RT, Graybiel AM, Desimone R, Boyden ES. 2009. Millisecond-timescale optical control of neural dynamics in the nonhuman primate brain. *Neuron* **62**:191–198. DOI: <https://doi.org/10.1016/j.neuron.2009.03.011>, PMID: 19409264
- Harsan LA, Dávid C, Reisert M, Schnell S, Hennig J, von Elverfeldt D, Staiger JF. 2013. Mapping remodeling of thalamocortical projections in the living reeler mouse brain by diffusion tractography. *PNAS* **110**:E1797–E1806. DOI: <https://doi.org/10.1073/pnas.1218330110>, PMID: 23610438
- Hau J, Sarubbo S, Perchey G, Crivello F, Zago L, Mellet E, Jobard G, Joliot M, Mazoyer BM, Tzourio-Mazoyer N, Petit L. 2016. Cortical Terminations of the Inferior Fronto-Occipital and Uncinate Fasciculi: Anatomical Stem-Based Virtual Dissection. *Frontiers in Neuroanatomy* **10**:58. DOI: <https://doi.org/10.3389/fnana.2016.00058>, PMID: 27252628
- Hunnigcutt BJ, Jongbloets BC, Birdsong WT, Gertz KJ, Zhong H, Mao T. 2016. A comprehensive excitatory input map of the striatum reveals novel functional organization. *eLife* **5**:e19103. DOI: <https://doi.org/10.7554/eLife.19103>, PMID: 27892854
- Jenkinson M, Smith S. 2001. A global optimisation method for robust affine registration of brain images. *Medical Image Analysis* **5**:143–156. DOI: [https://doi.org/10.1016/s1361-8415\(01\)00036-6](https://doi.org/10.1016/s1361-8415(01)00036-6), PMID: 11516708
- Jones DK. 2008. Tractography Gone Wild: Probabilistic Fibre Tracking Using the Wild Bootstrap With Diffusion Tensor MRI. *IEEE Transactions on Medical Imaging* **27**:1268–1274. DOI: <https://doi.org/10.1109/TMI.2008.922191>, PMID: 18779066
- Kaufman L, Kramer DM, Crooks LE, Ortendahl DA. 1989. Measuring signal-to-noise ratios in MR imaging. *Radiology* **173**:265–267. DOI: <https://doi.org/10.1148/radiology.173.1.2781018>, PMID: 2781018
- Krull A, Buchholz TO, Jug F. 2019. Noise2Void - Learning Denoising From Single Noisy Images. 2019 IEEE/CVF Conference on Computer Vision and Pattern Recognition (CVPR). DOI: <https://doi.org/10.1109/CVPR.2019.00223>
- Kuan L, Li Y, Lau C, Feng D, Bernard A, Sunkin SM, Zeng H, Dang C, Hawrylycz M, Ng L. 2015. Neuroinformatics of the Allen Mouse Brain Connectivity Atlas. *Methods (San Diego, Calif.)* **73**:4–17. DOI: <https://doi.org/10.1016/j.jymeth.2014.12.013>, PMID: 25536338
- Levy BJ, Wagner AD. 2011. Cognitive control and right ventrolateral prefrontal cortex: reflexive reorienting, motor inhibition, and action updating. *Annals of the New York Academy of Sciences* **1224**:40–62. DOI: <https://doi.org/10.1111/j.1749-6632.2011.05958.x>, PMID: 21486295
- Li A, Gong H, Zhang B, Wang Q, Yan C, Wu J, Liu Q, Zeng S, Luo Q. 2010. Micro-Optical Sectioning Tomography to Obtain a High-Resolution Atlas of the Mouse Brain. *Science* **330**:1404–1408. DOI: <https://doi.org/10.1126/science.1191776>, PMID: 21051596
- Liu D, Deng J, Zhang Z, Zhang Z-Y, Sun Y-G, Yang T, Yao H. 2020. Orbitofrontal control of visual cortex gain promotes visual associative learning. *Nature Communications* **11**:2784. DOI: <https://doi.org/10.1038/s41467-020-16609-7>, PMID: 32493971
- Luo L, Callaway EM, Svoboda K. 2018. Genetic Dissection of Neural Circuits: A Decade of Progress. *Neuron* **98**:256–281. DOI: <https://doi.org/10.1016/j.neuron.2018.03.040>, PMID: 29673479
- Lv Q, Yang L, Li G, Wang Z, Shen Z, Yu W, Jiang Q, Hou B, Pu J, Hu H, Wang Z. 2016. Large-Scale Persistent Network Reconfiguration Induced by Ketamine in Anesthetized Monkeys: Relevance to Mood Disorders. *Biological Psychiatry* **79**:765–775. DOI: <https://doi.org/10.1016/j.biopsych.2015.02.028>, PMID: 25837427
- Lv Q, Yan M, Shen X, Wu J, Yu W, Yan S, Yang F, Zeljik K, Shi Y, Zhou Z, Lv L, Hu X, Menon R, Wang Z. 2021. Normative Analysis of Individual Brain Differences Based on a Population MRI-Based Atlas of Cynomolgus Macaques. *Cerebral Cortex (New York, N.Y.)* **31**:341–355. DOI: <https://doi.org/10.1093/cercor/bhaa229>, PMID: 32844170
- Maier-Hein KH, Neher PF, Houde J-C, Côté M-A, Garyfallidis E, Zhong J, Chamberland M, Yeh F-C, Lin Y-C, Ji Q, Reddick WE, Glass JO, Chen DQ, Feng Y, Gao C, Wu Y, Ma J, He R, Li Q, Westin C-F, et al. 2017. The challenge of mapping the human connectome based on diffusion tractography. *Nature Communications* **8**:1349. DOI: <https://doi.org/10.1038/s41467-017-01285-x>, PMID: 29116093
- Markov NT, Ercsey-Ravasz MM, Ribeiro Gomes AR, Lamy C, Magrou L, Vezoli J, Misery P, Falchier A, Quilodran R, Gariel MA, Sallet J, Gamanut R, Huissoud C, Clavagnier S, Giroud P, Sappey-Marinié D, Barone P, Dehay C, Toroczkai Z, Knoblauch K, et al. 2014. A weighted and directed interareal connectivity matrix for macaque cerebral cortex. *Cerebral Cortex (New York, N.Y.)* **24**:17–36. DOI: <https://doi.org/10.1093/cercor/bhs270>, PMID: 23010748
- Mori S, Zhang J. 2006. Principles of diffusion tensor imaging and its applications to basic neuroscience research. *Neuron* **51**:527–539. DOI: <https://doi.org/10.1016/j.neuron.2006.08.012>, PMID: 16950152
- Mortazavi F, Oblak AL, Morrison WZ, Schmammann JD, Stanley HE, Wedeen VJ, Rosene DL. 2018. Geometric Navigation of Axons in a Cerebral Pathway: Comparing dMRI with Tract Tracing and Immunohistochemistry. *Cerebral Cortex (New York, N.Y.)* **28**:1219–1232. DOI: <https://doi.org/10.1093/cercor/bhx034>, PMID: 28203748
- Mukherjee P, Chung SW, Berman JL, Hess CP, Henry RG. 2008. Diffusion tensor MR imaging and fiber tractography: technical considerations. *AJNR. American Journal of Neuroradiology* **29**:843–852. DOI: <https://doi.org/10.3174/ajnr.A1052>, PMID: 18339719
- Mundell NA, Beier KT, Pan YA, Lapan SW, Göz Aytürk D, Berezovskii VK, Wark AR, Drokhlyansky E, Bielecki J, Born RT, Schier AF, Cepko CL. 2015. Vesicular stomatitis virus enables gene transfer and transsynaptic tracing in a wide range of organisms. *The Journal of Comparative Neurology* **523**:1639–1663. DOI: <https://doi.org/10.1002/cne.23761>, PMID: 25688551

- Naldini L**, Blömer U, Gallay P, Ory D, Mulligan R, Gage FH, Verma IM, Trono D. 1996. In Vivo Gene Delivery and Stable Transduction of Nondividing Cells by a Lentiviral Vector. *Science* **272**:263–267. DOI: <https://doi.org/10.1126/science.272.5259.263>, PMID: 8602510
- Nassi JJ**, Cepko CL, Born RT, Beier KT. 2015. Neuroanatomy goes viral! *Frontiers in Neuroanatomy* **9**:80. DOI: <https://doi.org/10.3389/fnana.2015.00080>, PMID: 26190977
- Neubert F-X**, Mars RB, Thomas AG, Sallet J, Rushworth MFS. 2014. Comparison of human ventral frontal cortex areas for cognitive control and language with areas in monkey frontal cortex. *Neuron* **81**:700–713. DOI: <https://doi.org/10.1016/j.neuron.2013.11.012>, PMID: 24485097
- Oh SW**, Harris JA, Ng L, Winslow B, Cain N, Mihalas S, Wang Q, Lau C, Kuan L, Henry AM, Mortrud MT, Ouellette B, Nguyen TN, Sorensen SA, Slaughterbeck CR, Wakeman W, Li Y, Feng D, Ho A, Nicholas E, et al. 2014. A mesoscale connectome of the mouse brain. *Nature* **508**:207–214. DOI: <https://doi.org/10.1038/nature13186>, PMID: 24695228
- Petrides M**. 2013. Neuroanatomy of Language Regions of the Human Brain. Academic Press.
- Ragan T**, Kadiri LR, Venkataraju KU, Bahlmann K, Sutin J, Taranda J, Arganda-Carreras I, Kim Y, Seung HS, Osten P. 2012. Serial two-photon tomography for automated ex vivo mouse brain imaging. *Nature Methods* **9**:255–258. DOI: <https://doi.org/10.1038/nmeth.1854>, PMID: 22245809
- Reveley C**, Seth AK, Pierpaoli C, Silva AC, Yu D, Saunders RC, Leopold DA, Ye FQ. 2015. Superficial white matter fiber systems impede detection of long-range cortical connections in diffusion MR tractography. *PNAS* **112**:E2820–E2828. DOI: <https://doi.org/10.1073/pnas.1418198112>, PMID: 25964365
- Reveley C**, Gruslys A, Ye FQ, Glen D, Samaha J, E Russ B, Saad Z, K Seth A, Leopold DA, Saleem KS. 2017. Three-Dimensional Digital Template Atlas of the Macaque Brain. *Cerebral Cortex (New York, N.Y)* **27**:4463–4477. DOI: <https://doi.org/10.1093/cercor/bhw248>, PMID: 27566980
- Rohlfing T**, Kroenke CD, Sullivan EV, Dubach MF, Bowden DM, Grant KA, Pfefferbaum A. 2012. The INIA19 Template and NeuroMaps Atlas for Primate Brain Image Parcellation and Spatial Normalization. *Frontiers in Neuroinformatics* **6**:27. DOI: <https://doi.org/10.3389/fninf.2012.00027>, PMID: 23230398
- Safadi Z**, Grisot G, Jbabdi S, Behrens TE, Heilbronner SR, McLaughlin NCR, Mandeville J, Versace A, Phillips ML, Lehman JF, Yendiki A, Haber SN. 2018. Functional Segmentation of the Anterior Limb of the Internal Capsule: Linking White Matter Abnormalities to Specific Connections. *The Journal of Neuroscience* **38**:2106–2117. DOI: <https://doi.org/10.1523/JNEUROSCI.2335-17.2017>, PMID: 29358360
- Sakagami M**, Pan X. 2007. Functional role of the ventrolateral prefrontal cortex in decision making. *Current Opinion in Neurobiology* **17**:228–233. DOI: <https://doi.org/10.1016/j.conb.2007.02.008>, PMID: 17350248
- Saleem KS**, Miller B, Price JL. 2014. Subdivisions and connective networks of the lateral prefrontal cortex in the macaque monkey. *The Journal of Comparative Neurology* **522**:1641–1690. DOI: <https://doi.org/10.1002/cne.23498>, PMID: 24214159
- Sani I**, McPherson BC, Stemmann H, Pestilli F, Freiwald WA. 2019. Functionally defined white matter of the macaque monkey brain reveals a dorso-ventral attention network. *eLife* **8**:e40520. DOI: <https://doi.org/10.7554/eLife.40520>, PMID: 30601116
- Sarubbo S**, Petit L, De Benedictis A, Chioffi F, Ptito M, Dyrby TB. 2019. Uncovering the inferior fronto-occipital fascicle and its topological organization in non-human primates: the missing connection for language evolution. *Brain Structure & Function* **224**:1553–1567. DOI: <https://doi.org/10.1007/s00429-019-01856-2>, PMID: 30847641
- Schambach A**, Zychlinski D, Ehrnstroem B, Baum C. 2013. Biosafety Features of Lentiviral Vectors. *Human Gene Therapy* **24**:132–142. DOI: <https://doi.org/10.1089/hum.2012.229>, PMID: 23311447
- Schmahmann JD**, Pandya DN. 2006. Fiber Pathways of the Brain. Oxford University Press. DOI: <https://doi.org/10.1093/acprof:oso/9780195104233.001.0001>
- Schmahmann JD**, Pandya DN, Wang R, Dai G, D'Arceuil HE, de Crespigny AJ, Wedeen VJ. 2007. Association fibre pathways of the brain: parallel observations from diffusion spectrum imaging and autoradiography. *Brain* **130**:630–653. DOI: <https://doi.org/10.1093/brain/awl359>, PMID: 17293361
- Sijbers J**, den Dekker AJ, Van Audekerke J, Verhoye M, Van Dyck D. 1998. Estimation of the noise in magnitude MR images. *Magnetic Resonance Imaging* **16**:87–90. DOI: [https://doi.org/10.1016/s0730-725x\(97\)00199-9](https://doi.org/10.1016/s0730-725x(97)00199-9), PMID: 9436952
- Stauffer WR**, Lak A, Yang A, Borel M, Paulsen O, Boyden ES, Schultz W. 2016. Dopamine Neuron-Specific Optogenetic Stimulation in Rhesus Macaques. *Cell* **166**:1564–1571. DOI: <https://doi.org/10.1016/j.cell.2016.08.024>, PMID: 27610576
- Stephan KE**. 2013. The history of CoCoMac. *NeuroImage* **80**:46–52. DOI: <https://doi.org/10.1016/j.neuroimage.2013.03.016>, PMID: 23523808
- Suárez LE**, Markello RD, Betzel RF, Misisic B. 2020. Linking Structure and Function in Macroscale Brain Networks. *Trends in Cognitive Sciences* **24**:302–315. DOI: <https://doi.org/10.1016/j.tics.2020.01.008>, PMID: 32160567
- Takemura H**, Pestilli F, Weiner KS, Keliris GA, Landi SM, Sliwa J, Ye FQ, Barnett MA, Leopold DA, Freiwald WA, Logothetis NK, Wandell BA. 2017. Occipital White Matter Tracts in Human and Macaque. *Cerebral Cortex (New York, N.Y)* **27**:3346–3359. DOI: <https://doi.org/10.1093/cercor/bhx070>, PMID: 28369290
- Tournier JD**, Calamante F, Connelly A. 2012. MRtrix: Diffusion tractography in crossing fiber regions. *International Journal of Imaging Systems and Technology* **22**:53–66. DOI: <https://doi.org/10.1002/ima.22005>
- Tournier JD**, Calamante F, Connelly A. 2013. Determination of the appropriate  $b$  value and number of gradient directions for high-angular-resolution diffusion-weighted imaging. *NMR in Biomedicine* **26**:1775–1786. DOI: <https://doi.org/10.1002/nbm.3017>, PMID: 24038308

- van den Heuvel MP**, de Reus MA, Feldman Barrett L, Scholtens LH, Coopmans FMT, Schmidt R, Preuss TM, Rilling JK, Li L. 2015. Comparison of diffusion tractography and tract-tracing measures of connectivity strength in rhesus macaque connectome. *Human Brain Mapping* **36**:3064–3075. DOI: <https://doi.org/10.1002/hbm.22828>, PMID: 26058702
- Wang Z**, Chen LM, Négyessy L, Friedman RM, Mishra A, Gore JC, Roe AW. 2013. The relationship of anatomical and functional connectivity to resting-state connectivity in primate somatosensory cortex. *Neuron* **78**:1116–1126. DOI: <https://doi.org/10.1016/j.neuron.2013.04.023>, PMID: 23791200
- Watakabe A**, Ohtsuka M, Kinoshita M, Takaji M, Isa K, Mizukami H, Ozawa K, Isa T, Yamamori T. 2015. Comparative analyses of adeno-associated viral vector serotypes 1, 2, 5, 8 and 9 in marmoset, mouse and macaque cerebral cortex. *Neuroscience Research* **93**:144–157. DOI: <https://doi.org/10.1016/j.neures.2014.09.002>, PMID: 25240284
- Wedeen VJ**, Rosene DL, Wang R, Dai G, Mortazavi F, Hagmann P, Kaas JH, Tseng W-YI. 2012. The geometric structure of the brain fiber pathways. *Science (New York, N.Y.)* **335**:1628–1634. DOI: <https://doi.org/10.1126/science.1215280>, PMID: 22461612
- Zeng H**. 2018. Mesoscale connectomics. *Current Opinion in Neurobiology* **50**:154–162. DOI: <https://doi.org/10.1016/j.conb.2018.03.003>, PMID: 29579713
- Zhan Y**, Wei J, Liang J, Xu X, He R, Robbins TW, Wang Z. 2021. Diagnostic Classification for Human Autism and Obsessive-Compulsive Disorder Based on Machine Learning From a Primate Genetic Model. *The American Journal of Psychiatry* **178**:65–76. DOI: <https://doi.org/10.1176/appi.ajp.2020.19101091>, PMID: 32539526
- Zhang Z**, Cai DC, Wang Z, Zeljic K, Wang Z, Wang Y. 2019. Isoflurane-Induced Burst Suppression Increases Intrinsic Functional Connectivity of the Monkey Brain. *Frontiers in Neuroscience* **13**:296. DOI: <https://doi.org/10.3389/fnins.2019.00296>, PMID: 31031580
- Zingg B**, Hintiryan H, Gou L, Song MY, Bay M, Bienkowski MS, Foster NN, Yamashita S, Bowman I, Toga AW, Dong H-W. 2014. Neural networks of the mouse neocortex. *Cell* **156**:1096–1111. DOI: <https://doi.org/10.1016/j.cell.2014.02.023>, PMID: 24581503